Biochemical Engineering Journal 177 (2022) 108265

Contents lists available at ScienceDirect

Biochemical Engineering Journal

journal homepage: www.elsevier.com/locate/bej

Computational fluid dynamics modelling of hydrodynamics, mixing and oxygen transfer in industrial bioreactors with Newtonian broths

Gisela Nadal-Rey [a,b], Dale D. McClure [c], John M. Kavanagh [c], Benny Cassells [b], Sjef Cornelissen [b,1], David F. Fletcher [c], Krist V. Gernaey [a,*]

[a] Process and Systems Engineering Center (PROSYS), Department of Chemical and Biochemical Engineering, Technical University of Denmark, Building 228 A, 2800 Kgs. Lyngby, Denmark
[b] Novozymes A/S, Fermentation Pilot Plant, Krogshoejvej 36, 2880 Bagsvaerd, Denmark
[c] The University of Sydney, School of Chemical and Biomolecular Engineering, Building J01, Camperdown 2006, NSW, Australia

ARTICLE INFO

Keywords:
Computational Fluid Dynamics Modelling
Large-Scale Bioreactor
Hydrodynamics
Oxygen Transfer
Mixing
Newtonian Broth

ABSTRACT

Industrial aerobic fermentation processes are performed in large-scale bioreactors (> 20 m^3). Understanding the local values of the velocity field, the eddy dissipation rate and the gas volume fraction is of interest, as these parameters affect mixing and mass transfer and hence fermentation process performance and profitability. Despite the industrial and academic importance of these flow variables in large-scale bioreactors, there is scarce literature addressing it. This article provides a numerical comparison using Computational Fluid Dynamics (CFD) of different industrially relevant reactor types (bubble columns and stirred tanks with different impeller configurations) operated within a realistic range of industrial conditions (40 – 90 m^3, 0.3 – 6 kW m^{-3}, 0.5 – 1 vvm). Local flow variables and mixing times are evaluated for all cases studied. The collection of these data allows the prediction of the typical values of mixing time (10 – 206 s) and oxygen transfer rate (1 – 8 kg m^{-3} h^{-1}) in industrial bioreactors, and serves as basis for the comparison between different reactor types.

1. Introduction

Industrial-scale fermentation processes are widely used to produce a diverse range of compounds with applications in the food, chemical and pharmaceutical industries [1]. Therefore, understanding the behaviour of large-scale bioreactors is a topic of considerable industrial importance. Typical industrial processes are operated in fed-batch mode [2], meaning the liquid volume changes substantially over the course of the batch.

Most industrial-scale aerobic bioreactors are typically either bubble columns or stirred tanks [1]. Of the two designs, bubble columns are simpler; air is introduced through a sparger at the base of the column and this provides both mixing and a source of oxygen. In addition to the sparger, stirred tanks have an agitator which provides mixing. Agitators are typically classified based on whether they pump the liquid axially or radially. Rushton turbines are a commonly used radial flow impeller design, while a range of axial flow impellers exist [3]. Industrial-scale reactors typically have multiple (2–4) impellers, common configurations are four Rushton turbines, or one Rushton turbine at the lowest position and multiple axial flow impellers above it [4]. The internal structure of stirred tanks is also more complex than bubble columns, as it is typically necessary to include baffles to prevent vortex formation [3].

Understanding the hydrodynamics inside industrial bioreactors is important as this governs the mixing and mass transfer inside the reactor. As mass transfer limits most processes, key metrics like the yield and productivity may be affected. For example, it is well known [5–8] that gradients in substrate concentration can affect the overall process yield, and that the extent of these gradients is directly related to mixing within the reactor. Similarly, understanding oxygen transfer is key for aerobic fermentation processes. Oxygen is sparingly soluble (of the order 8 mg L^{-1} at atmospheric pressure [1]), making its supply the limiting factor in many industrial aerobic fermentation processes. Hence, the productivity of large-scale aerobic fermentation processes is often directly related to the oxygen transfer rate.

Due to the two-phase (gas-liquid) nature of the flow, the hydrodynamics inside industrial bioreactors is complex and challenging to model [9,10]. These challenges are compounded by the fact that the fermentation medium is a complex mixture containing a range of components which can affect hydrodynamics and mass transfer [11,12]. Despite

* Corresponding author.
E-mail address: kvg@kt.dtu.dk (K.V. Gernaey).
[1] Currently at: Centrient Pharmaceuticals, Alexander Fleminglaan 1, 2613 AX Delft, The Netherlands

https://doi.org/10.1016/j.bej.2021.108265
Received 6 May 2021; Received in revised form 3 October 2021; Accepted 29 October 2021
Available online 3 November 2021

Nomenclature

Abbreviations

A310	stirred tank with one Rushton turbine disk impeller at the bottom and hydrofoil A310 impellers at the top
BC	bubble column
BM	benchmark conditions
CFD	Computational Fluid Dynamics
LS	low settings conditions
RMS	root mean square
RTD	stirred tank with Rushton turbine disk impeller

Roman letters

a	interfacial area for mass transfer [m^2 m^{-3}]
C_1	constant [-]
C_2	constant [-]
C_μ	constant [-]
d_b	bubble diameter [m]
$d_{b,out}$	bubble diameter at the outlet [m]
$D_{L\phi}$	kinematic diffusivity of the tracer in the liquid [m^2 s^{-1}]
D_{O2}	diffusivity of oxygen in water [m^2 s^{-1}]
g	gravitational constant or vector [m s^{-2}]
G	gas phase
H	total mixture height [m]
H	Henry's law constant [Pa m^3 mol^{-1}]
k	isentropic exponent for air compression [-]
k_L	liquid film mass transfer coefficient [m s^{-1}]
$k_L a$	overall mass transfer coefficient [h^{-1}]
L	liquid phase
M_{GL}	inter-phase momentum transfer term [kg m^{-2} s^{-2}]
N	agitation speed [s-1]
O	dissolved oxygen concentration [kg m^{-3}]
O^*	oxygen concentration at saturation [kg m^{-3}]
OTR	oxygen transfer rate [kg m^{-3} h^{-1}]
p	pressure [Pa]
P_{abs}	absolute pressure [Pa]
P_{atm}	atmospheric pressure [Pa]
P_c	power consumption from air compression [W]
P_{head}	headspace pressure [Pa]
P_i	power input for agitation [kW m^{-3}]
P_{in}	sparger inlet pressure [Pa]
P_L	production of turbulence due to shear [kg m^{-1} s^{-3}]
P_{ref}	reference pressure [Pa]
Q_G	air flow rate [m^3 s^{-1}]
$S_{ct,L}$	liquid-phase turbulent Schmidt number [-]
$S_{L\phi}$	source term for tracer addition [kg m^{-3} s^{-1}]
t	time [s]
T_{imp}	impeller torque [N m]
$T_{LG,k}$	source term for bubble-induced turbulence [kg m^{-1} s^{-3}]
$T_{LG,\varepsilon}$	source term for bubble-induced turbulence [kg m^{-1} s^{-4}]
U	velocity [m s^{-1}]
V_L	liquid volume [m^3]
V_T	total mixture volume [m^3]
y	mole fraction of oxygen in the gas phase [-]

Greek letters

α	volume fraction [-]
Γ	term accounting for inter-phase mass transfer [kg m^{-3} s^{-1}]
$\boldsymbol{\delta}$	Dirac delta function [-]
ε	eddy dissipation rate [m^2 s^{-3}]
μ_{eff}	effective viscosity [Pa s]
$\mu_{t,L}$	turbulent viscosity in the liquid phase [Pa s]
ρ	density [kg m^{-3}]
σ_k	constant [-]
σ_ε	constant [-]
φ_L	tracer quantity per mass of liquid [kg kg^{-1}]

these challenges, Computational Fluid Dynamics (CFD) is increasingly [13–17] being used as a tool to model fluid flow behaviour inside bioreactors as CFD can provide an extremely high level of detail of all types of flow variables (e.g., velocity, pressure). However, only few studies (e.g. [4,17]) have examined industrial scale vessels, which can be up to 1000 m^3 in volume [18], and few systematic comparisons between different reactor configurations exist in the open literature.

A widely used metric to quantify the mixing performance is the mixing time. This is generally taken as the time for the concentration of a tracer to reach ± 5% of the equilibrium value [1]. Ideally, the mixing time would be as low as possible, as this would mean that the substrates are likely to be rapidly and uniformly distributed throughout the reactor. It has been shown that for bubble columns the measured mixing time depends on both the location where the tracer is added and the location where its concentration is measured [19]. The superficial gas velocity has minimal influence on the mixing time for velocities greater than 0.07 m s^{-1} [19–21]. Another interesting observation regarding mixing in bubble columns is that due to the transient nature of the flow, the mixing time is sensitive to the initial flow pattern when the tracer is added. Hence, a more representative quantitation of the mixing time may involve adding multiple tracers and calculating the average mixing time and the standard deviation [19].

The mixing behaviour of stirred tanks has been shown to be largely influenced by the impeller configuration [4]. This behaviour arises because having multiple radial flow impellers can create barriers to axial flow, thereby reducing the mixing within the system. Interestingly, such barriers do not exist in a bubble column, meaning that such a configuration may have improved mixing performance in comparison with stirred fermenters equipped with multiple radial impellers.

Oxygen transfer (*OTR*) within a bioreactor is a function of the oxygen saturation concentration (O^*), the liquid film mass transfer coefficient (k_L) and the interfacial area for mass transfer (a) as shown in Eq. (1):

$$OTR = k_L a(O^* - O) \tag{1}$$

Values of k_L and the a depend on the eddy dissipation rate (ε), with higher values leading to bubble break-up (and hence increased gas-liquid interfacial area and increased values of k_L). In some instances (e.g. mammalian cell cultures), avoiding high values of ε may be important in limiting hydrodynamic damage to cells [1].

The presence of surface-active compounds (e.g. antifoam agents or other compounds found in fermentation media) can significantly affect the process by reducing oxygen transfer by a factor of 3–5 by influencing the value of k_L [12,22,23]. This reduction may change over the course of a batch as compounds accumulate (e.g. by-products) or get diluted (e.g. media components) in the liquid phase. Due to these phenomena, the mathematical description of k_L can become challenging in such industrial systems.

Finally, another aspect influencing the oxygen transfer rate has been found to be the reactor type. Humbird et al. [24] compared oxygen transfer in bubble columns and stirred tank reactors using correlations from the literature for oxygen uptake rates up to 150 mmol L^{-1} h^{-1} (4.8 kg m^{-3} h^{-1}), finding that the cost of oxygen delivery was approximately 10–20% less for the bubble columns operating at comparable OTR levels.

A challenge when comparing different bioreactor configurations is the lack of published data for measurements made at industrially

relevant scales and conditions. Such data are rarely available due to both practical and commercial considerations. Hence, the aim of this work is to use CFD modelling to compare different large-scale reactor configurations with the aim of quantifying their performance in terms of mixing and oxygen transfer.

2. Methodology

2.1. Geometries and meshes

In this work three different reactor configurations were modelled: a bubble column, a stirred tank with four Rushton impellers and a stirred tank with one Rushton impeller and three hydrofoil A310 impellers. These configurations have been selected on the basis that they are representative of widely used industrial bioreactors [4,25,26]. Schematics showing the reactor configurations with their dimensions are given in Fig. 1A-B and E-F. Simulations were made at volumes of 40, 60 and 90 m^3, corresponding to the beginning, middle and end of an industrial fed-batch fermentation process.

The mesh used for simulations of the bubble column was generated with Ansys meshing 2019R2, as it can generate swept meshes, and is shown in Fig. 1 G. The same mesh was used for all cases with the liquid

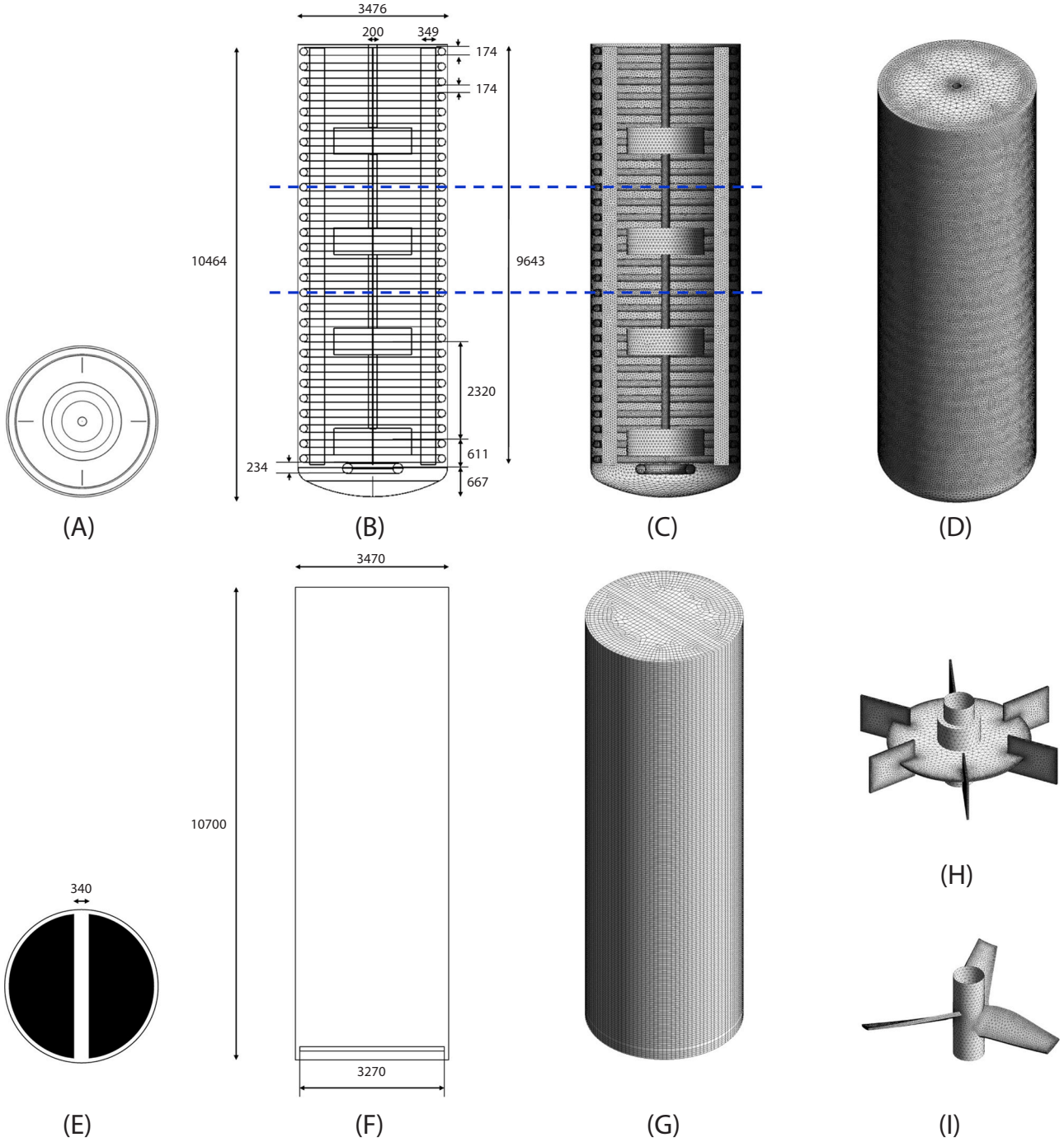

Fig. 1. Schematics of the geometry used with all relevant measurements (in mm) for the 90 m^3 volume of the tank domain of the stirred tanks (A and B) and the bubble columns (E and F). XY view of the internal surface mesh for the 90 m^3 volume of the tank domain of the stirred tanks (C). Isometric perspectives of the 90 m^3 mesh for the stirred tanks (D) and bubble columns (G), and of the two types of impellers used: a Rushton turbine disk (H) and a hydrofoil A310 (I).

height being varied to obtain the correct liquid volume. A step function was used to initialise the simulation, below the liquid height the liquid volume fraction was set to one, while above the initial liquid level the liquid phase volume fraction was zero. Initial liquid heights of 3.38, 4.85 and 6.73 m were used for the 40, 60 and 90 m^3 cases, respectively. For the stirred tank reactors, the meshes were changed to increase the computational efficiency (Fig. 1C).

As shown in Fig. 1C and D, the meshes for the stirred tank configurations were more complex due to the need to model the internals (cooling coil and baffles). The meshes were created using Ansys Fluent Meshing 2019 R3, as this generates much better quality tetrahedral meshes than Ansys Meshing, and were divided into two domains, one for the tank (stator) and the other for the impeller (rotor). The surface meshes of the impeller types used are shown in Fig. 1H and I. The number of mesh elements for all case studies is summarized in Table 1. The locations of the planes used to display the results are shown in Fig. 2. Section 2 of the Supplementary Material provides a detailed comparison between the model predictions for the STR with two Rushton impellers for three different grid sizes (2.2×10^6, 3.4×10^6 and 4.2×10^6 elements). It was found that predictions of the gas volume fraction, liquid velocity in the stationary frame, turbulence kinetic energy and turbulence eddy dissipation were not dependent on the grid size. The grid sizing for the bubble column simulations has been based on our previous work [27] where it was shown that use of a similar sized mesh gave grid-independent results.

To model the impeller rotation a number of approaches are available. In many applications it is possible to solve the equations in a zone around the impeller in a rotating frame of reference and couple the rotating and stationary zones using assumptions of either a fixed relative location of the impeller (Frozen Rotor) or by averaging quantities circumferentially on the zone interface (Stage Average). These methods are computationally cheaper as they can be run steady state, but they need a relatively open geometry to work well. We tried them initially and found very poor convergence as the blade tips are close to the coils. Therefore, we performed all calculations in a transient manner with the inner mesh rotating in a sliding mesh approach (Transient Rotor Stator). This is the most accurate method but is also computationally expensive even though Ansys CFX provides good parallelisation of the data transfer.

2.2. Computational fluid dynamics (CFD) modelling

In this work the Euler-Euler approach was used to model the two-phase (gas-liquid) flow. Conservation equations for mass and momentum for both the gas and liquid phases are given in Eq. (2-5):

$$\frac{\partial(\rho_G \alpha_G)}{\partial t} + \nabla\bullet\,(\rho_G \alpha_G \boldsymbol{U}_G) = -\Gamma_{GL} \tag{2}$$

$$\frac{\partial(\rho_L \alpha_{GL})}{\partial t} + \nabla\bullet\,(\rho_L \alpha_L \boldsymbol{U}_L) = \Gamma_{GL} \tag{3}$$

$$\frac{\partial(\rho_G \alpha_G \boldsymbol{U}_G)}{\partial t} + \nabla\bullet\,(\rho_G \alpha_G \boldsymbol{U}_G \otimes \boldsymbol{U}_G) = -\alpha_G \nabla p + \nabla\bullet\left(\alpha_G \mu_{G,\,\mathrm{eff}}\left[\nabla \boldsymbol{U}_G + (\nabla \boldsymbol{U}_G)^T - \frac{2}{3}\boldsymbol{\delta}\nabla.\boldsymbol{U}_G\right]\right) + \alpha_G \rho_G \boldsymbol{g} + \boldsymbol{M}_{GL} - \Gamma_{GL}\boldsymbol{U}_G \tag{4}$$

$$\frac{\partial(\rho_L \alpha_L \boldsymbol{U}_L)}{\partial t} + \nabla\bullet\,(\rho_L \alpha_L \boldsymbol{U}_L \otimes \boldsymbol{U}_L) = -\alpha_L \nabla p + \nabla\bullet\left(\alpha_G \mu_{L,\,\mathrm{eff}}\left[\nabla \boldsymbol{U}_L + (\nabla \boldsymbol{U}_L)^T - \frac{2}{3}\boldsymbol{\delta}\nabla.\boldsymbol{U}_L\right]\right) + \alpha_L \rho_L \boldsymbol{g} - \boldsymbol{M}_{GL} + \Gamma_{GL}\boldsymbol{U}_G \tag{5}$$

where ρ is the density, α is the volume fraction, $\boldsymbol{U}$ is the velocity, Γ is the term accounting for inter-phase mass transfer, p is the pressure, μ_{eff} is the effective viscosity, $\boldsymbol{\delta}$ is the Dirac delta function, $\boldsymbol{g}$ is the gravitational acceleration vector, t is the time and $\boldsymbol{M}_{GL}$ is the inter-phase momentum transfer term. The subscripts G and L refer to the gas and liquid phases, respectively.

Inter-phase momentum transfer was modelled as the sum of drag and turbulent dispersion. The Favre-averaged drag model developed by Burns et al. [28] was used to model turbulent dispersion. Following our previous work [29–31], the drag in the bubble column was modelled using the drag correlation for an isolated bubble developed by Grace et al. [32] in combination with a modified [29,30] form of the volume fraction correction term developed by Simonnet et al. [33] to account for the presence of surfactants in the liquid phase. The drag correlation developed by Ishii and Zuber [34] was used in modelling the stirred tank reactors.

Liquid-phase turbulence was modelled using the standard k-ε model. The transport equations for turbulence kinetic energy (k) and turbulence kinetic energy dissipation rate (ε) are shown in Eqs. (6) and (7), respectively:

$$\frac{\partial(\alpha_L \rho_L k_L)}{\partial t} + \nabla\bullet\left(\alpha_L\left(\rho_L k_L \boldsymbol{U}_L - \left(\mu_L + \frac{\mu_{t,L}}{\sigma_k}\right)\nabla k_L\right)\right) = \alpha_L(P_L - \rho_L \varepsilon_L) + T_{LG,k} \tag{6}$$

$$\frac{\partial(\alpha_L \rho_L \varepsilon_L)}{\partial t} + \nabla\bullet\left(\alpha_L\left(\rho_L \varepsilon_L \boldsymbol{U}_L - \left(\mu_L + \frac{\mu_{t,L}}{\sigma_\varepsilon}\right)\nabla \varepsilon_L\right)\right) = \alpha_L \frac{\varepsilon_L}{k_L}(C_1 P_L - C_2 \rho_L \varepsilon_L) + T_{LG,\varepsilon} \tag{7}$$

where C_1, C_2, σ_k and σ_ε are constants that have the standard values of 1.44, 1.92, 1.0 and 1.3, respectively [35]. P_L is the production of turbulence due to shear and $T_{LG,k}$ and $T_{LG,\varepsilon}$ are source terms which account for bubble-induced turbulence. The model developed by Yao and Morel [36] was used to account for the bubble-induced turbulence. Turbulent viscosity in the liquid phase ($\mu_{t,L}$) was calculated using:

$$\mu_{t,L} = C_\mu \rho_L \left(\frac{k_L^2}{\varepsilon_L}\right) \tag{8}$$

where the constant C_μ has a value of 0.09 [35]. Turbulence in the gas phase was modelled using the dispersed phase zero equation approach.

As previously noted, the presence of surface-active compounds in fermentation medium tends to favour a narrow bubble size distribution [37], for this reason a single bubble size was used. Such an approach also has the advantage of increased computational efficiency [38]. Given the size of the reactors being modelled, the expansion of the gas due to the change in pressure is significant; hence the bubble diameter (d_b) was

Table 1
Number of mesh elements of all CFD models utilized.

Case study	Impeller configuration	Mesh elements × 10^5
Bubble column	n.a.	2.71
Stirred tank, 40 m^3	2 RTD	34.3
	1 RTD + 1 A310	24.4
Stirred tank, 60 m^3	3 RTD	52.9
	1 RTD + 2 A310	32.1
Stirred tank, 90 m^3	4 RTD	70.9
	1 RTD + 3 A310	41.2

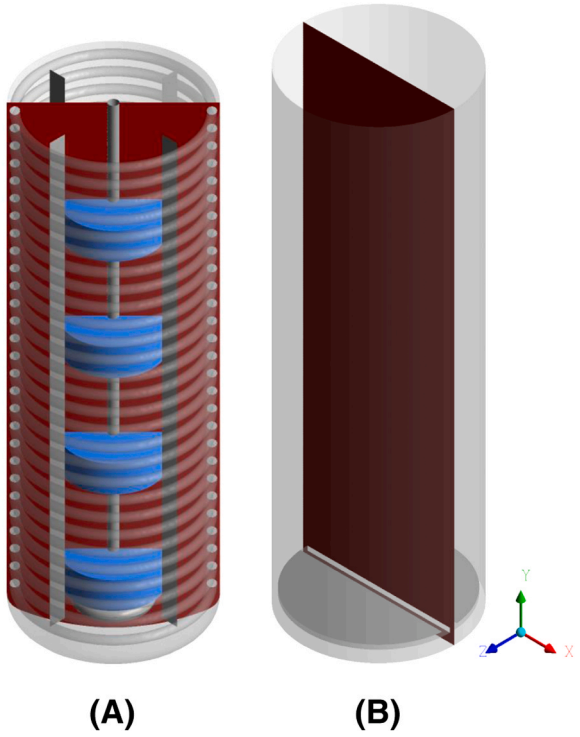

Fig. 2. Location of the planes (in red) used to display the CFD results for all the stirred tank (A) and bubble column (B) cases studied. Although only the largest volume has been depicted, the same plane is used for all volumes that have been simulated. In blue, the interfaces between tank and impeller domains are shown. In grey, the walls and internals of the fermenters are represented.

made a function of the pressure (which is primarily related to the height within the reactor):

$$d_b = d_{b,out}\sqrt[3]{\frac{P_{\text{ref}}}{P_{\text{abs}}}} \tag{9}$$

where P_{ref} is the reference pressure (1 atm) and P_{abs} is the absolute pressure. The bubble diameter at the outlet ($d_{b,\text{out}}$) was set to be 5 mm, this value being based on experimental measurements of the bubble size in fermentation medium [37].

The liquid phase was assumed to be a Newtonian fluid to simulate bacterial and yeast fermentation broth. A value of 1050 kg m^{-3} was used for the liquid density, this value being chosen to be representative of fermentation broth [39]. To mimic the increase in cell density of an industrial fed-batch fermentation process [40], the viscosity was increased for the simulations at larger volumes. Values of 0.692, 2.08 and 4.14 mPa s were used for the 40, 60 and 90 m^3 cases, respectively. These values are based on measurements of yeast fermentation broth at increasing cell densities (up to 150 g L^{-1}) [40]. Properties for air at 25 °C were used for the gas phase. For the stirred tanks, the air density was calculated following the ideal gas law. It was assumed that the processes were isothermal (i.e., no energy equations were solved).

To correctly model the two-phase flow in industrial bioreactors it was necessary to model the system as a transient with small time-steps with a relatively long averaging time (90 s). A fixed value of 1 ms was used for the bubble column simulations, while values of 5–10 ms were used for the stirred tank systems, these being calculated such that the impeller rotation did not exceed more than 5° per timestep. This value is chosen as a compromise between long solution times (smaller values) and poor resolution (often associated with excessive numbers of iterations per time step) and sits within the range of values reported elsewhere [41]. The Courant number was less than unity for most computational cells and convergence was obtained in typically 2–3 sub-iterations per timestep, confirming the choice of timestep. By doing that, a representative timescale was calculated, so all transient phenomena could be modelled appropriately. The agitation rate values used for all stirred tank cases are summarized in Table 2.

Two sets of operational conditions were evaluated for all bioreactor types and volumes. These corresponded to benchmark (i.e., standard) conditions and low settings. The operational variables which varied between conditions were the air flow rate, the volumetric power input used for agitation (P_i/V_L) and the headspace pressure. A summary of the settings used in all simulations performed is provided in Table 2. The volumetric power input from the impellers (P_i/V_L) was monitored as an

Table 2
Summary of simulations performed with their operational settings. N is the agitation rate and P_i/V_L is the power input per volume from agitation.

Reactor type	Operational conditions	Volume [m^3]	Air flow rate [kg s^{-1}]	N [rpm]	$\frac{P_i}{V_L}$[kW m^{-3}]	Headspace pressure [bar]
Bubble column	Benchmark	44	0.87	n.a.		0
		63	1.31			
		88	1.93			
	Low settings	43	0.44			
		64	0.65			
		89	0.97			
Stirred tank, RTDs	Benchmark	40	0.79	110	4.3	1
		60		115	4.1	
		90		140	3.9	
	Low settings	40	0.40	60	0.9	0
		60		70	0.9	
		90		80	0.9	
Stirred tank, RTD + A310s	Benchmark	40	0.79	140	4.2	1
		60		160	4.2	
		90		180	4.0	
	Low settings	40	0.40	80	1.0	0
		60		90	0.9	
		90		100	0.8	

expression during the solving of the CFD simulations with the following mathematical expression:

$$\frac{P_i}{V_L} = \frac{\sum T_{Imp} \times 2 \times \pi \times N}{V_T \times (1 - \alpha_G)} \tag{10}$$

where T_{Imp} corresponds to the torque of each impeller (computed using an in-built function in Ansys CFX that integrates the vector product of distance from the axis and the force on the face over the object of interest, in this case the impellers), N to the agitation rate, V_T to the total mixture volume and α_G to the gas volume fraction. Preliminary simulations were performed where N was varied to determine values that would give the desired volumetric power input.

For both the bubble column and stirred tank configurations the sparger design was simplified to reduce the mesh size. As shown in Fig. 1E the air was introduced in two locations in the bubble column, this being done as a simplification of a 'tree' type sparger (a commonly used industrial configuration). A ring sparger was used for the stirred tank cases. In both cases, air was introduced at the top face of the sparger; both designs are shown in Fig. 1 A and E. Air was introduced at a fixed mass flow rate, for the bubble columns, this was varied based on the volume and corresponded to 0.5 vvm for the low settings case and 1 vvm for the benchmark settings. In contrast, the volumetric flow rate for the stirred tank reactors was set at 0.5 or 1 vvm at the initial volume (40 m^3), and it was kept constant for the other volumes to prevent impeller flooding. A summary of the mass flow rates used for all cases studied is provided in Table 2.

The power consumption from air compression (P_c) was calculated assuming single stage, isentropic and adiabatic compression of the volumetric air flow rate (Q_G) from atmospheric pressure (P_{atm}) to sparger inlet pressure (P_{in}) as described in Eq. (11):

$$P_c = \frac{k}{k-1} Q_G P_{atm} \left(\left(\frac{P_{in}}{P_{atm}} \right)^{\frac{k-1}{k}} - 1 \right) \tag{11}$$

where k is the isentropic exponent for air compression with a value of 1.4 [42]. P_{in} is calculated as the summation of the hydrostatic pressure, the atmospheric pressure and the headspace pressure (P_{head}) (if applicable) as shown in Eq. (12):

$$P_{in} = P_{head} + P_{atm} + \rho_L \times g \times h \times (1 - \alpha_G) \tag{12}$$

where h is the height of the two-phase mixture. The total power input was calculating by adding the power input for agitation purposes (P_i) and the power input for air compression (P_c).

Wall boundary conditions (in the stirred tanks, also including internal hardware) were modelled as free slip for the gas phase and no slip for the liquid. In the stirred tank cases, the transient rotor-stator frame change model was used to describe the interface between the rotation (impeller) and stationary (tank) domains. The column outlet was modelled as an opening, at zero gauge pressure. In contrast, the outlet of the stirred tank reactors was modelled using the degassing boundary condition.

To test the validity of the degassing boundary condition, the stirred tank mesh with Rushton turbine disks of the 40 m^3 case with low settings was extended in the vertical axis and a simulation was performed with the same type of outlet as the bubble column. Both simulation results with different outlet boundary conditions presented good agreement in terms of velocity field, gas volume fraction and power input per liquid volume (see Supplementary Material 1). Nevertheless, although the pressure difference with the degassing boundary condition was correct, the absolute pressure drifted, resulting in significantly lower absolute pressure values. This phenomenon also occurred in almost all stirred tank cases, as a result of the use of a degassing boundary condition in a transient setup where it was unable to adjust the pressure properly. This pressure inconsistency did not affect the magnitude and pattern of the fluid flow nor the gas volume fraction, as validated with the numerical test. Thus, the absolute pressure values were corrected when post-processing the CFD simulation results for hydrodynamics. The hydrostatic pressure was calculated and used for the estimation of the bubble diameter (Eq. 9), and of the oxygen concentration at saturation (Eq. 16). The average differences between the corrected and non-corrected bubble diameter and oxygen concentration at saturation values correspond to 6% and 12%, respectively. The degassing boundary condition was initially selected with the aim of minimising the computational burden, and this approach is commonly used in bioreactor systems [16,17]. However, in this work it is concluded that it is not an appropriate choice in transient setup. Instead, an opening at zero gauge pressure at the top of a free space is recommended as a good CFD modelling practice.

Simulations were set up and solved using Ansys CFX 19.2. The coupled solver was used for the momentum equations and included the volume fraction equations, the high-resolution advection scheme was used combined with a first-order scheme for the turbulence equations and the second-order backward Euler scheme for the transient terms. A target of 1×10^{-4} was set for the RMS residuals, and this was typically reached within 3–5 coefficient loops for the bubble columns and 5–10 coefficient loops for the stirred tank cases. For both cases simulations were run for a time period of 30 s, this being done to initialise the fluid flow. After this 30 s transient averaging was turned on for the velocity, gas volume fraction and turbulence variables and the simulations were run for an additional 90 s.

Six scalar variables were included to act as tracers. Liquid-phase mixing was modelled using the transport equation for a scalar:

$$\frac{\partial(\alpha_L \rho_L \varphi_L)}{\partial t} + \nabla \bullet (\alpha_L \rho_L \boldsymbol{U}_L \varphi_L) - \nabla \bullet \left(\alpha_L \left(\rho_L D_L^{\varphi} + \frac{\mu_{t,L}}{Sc_{t,L}} \right) \nabla \varphi \right) = S_L^{\varphi} \tag{13}$$

where φ is the tracer quantity per mass of liquid, D_L^{φ} is the kinematic diffusivity of the tracer in the liquid and S_L^{φ} is the source term that accounts for tracer addition. The liquid-phase turbulent Schmidt number ($Sc_{t,L}$) was set to the default value (0.9). A value of 8.5×10^{-10} m^2 s^{-1} was used for the kinematic diffusivity of the tracer, this value being equivalent to the diffusivity of glucose in water [2]. Tracers were introduced for a period of 1 s at a feed rate of 312 kg s^{-1}. The source points for tracer addition are shown in Fig. 8A. Three tracers were introduced at each source point. The mixing time was defined as the time taken for the tracer concentration to be within ± 5% of the equilibrium value [1]. In Fig. 8B and C, reported values of the mixing time are the average of the three replicate measurements, with error bars denoting one standard deviation about the mean. In Fig. 11A, the averages and standard deviations of the mixing time values for one configuration and volume have been calculated based on the six measurements considering both top and bottom feeding positions.

The oxygen transfer rate (OTR) was calculated as in Eq. (1). The interfacial area a has been calculated based on the local bubble diameter and volume fraction:

$$a = \frac{6\alpha_G}{d_b} \tag{14}$$

Two approaches have been used to calculate k_L. Firstly, a constant value (2×10^{-4} m s^{-1}, measured for surfactant containing systems [43]) was used; in the second approach the correlation developed by Lamont and Scott [44] was used to calculate k_L:

$$k_L = 0.4 D_{O2}^{0.5} \left(\frac{\varepsilon \rho_L}{\mu_L} \right)^{0.25} \tag{15}$$

where D_{O2} is the diffusivity of oxygen in water (2.42×10^{-9} m^2 s^{-1} at 25 °C [2]). Henry's law was used to calculate the value of O^*:

$$O^* = \frac{y P_{abs}}{H} \tag{16}$$

where y is the mole fraction of oxygen in air and H is the Henry's law constant in water (77,007 Pa m^3 mol^{-1} at 25 °C [2]). Effects of the liquid phase composition on the value of H were not taken into account.

The volume-average transient average values of the OTR were calculated based on the volume- weighted transient average values of O^*, k_L and a, following Eq. (1).

2.3. Verification and validation

It is important that any model undergoes rigorous verification and validation. The use of a highly respected CFD solver (Ansys CFX) means that extensive verification and validation is carried out by the vendors and development follows strict QA standards. In addition to that we have carried out extensive work ourselves to ensure the models are implemented correctly and provide a good representation of the physics. We note however that most validation has been done for laboratory-scale systems because of the challenges of collecting data for large-scale systems and when undertaken it has significant commercial value and is generally not published in the open literature.

The model used for the bubble column simulations has undergone extensive validation at the bench-top [45] and pilot [19,31,46] scales, including a rigorous comparison between the results from two commercially available codes (Ansys CFX and Fluent) [29]. Additionally, the model has been validated [27] against experimental data from large (up to 3 m diameter) columns.

The ability of Ansys CFX to model flow in stirred tanks has been studied extensively and there are numerous published works that investigate the various solution methods and modelling approaches. For example, the modelling of flow generated by Rushton turbines in baffled vessels is addressed in [41]. The simulation of mixing times and bubble-induced mass transfer has been studied and compared with experimental data for a pilot reactor [47], with this paper showing it was possible to achieve good agreement between experimental measurements and CFD predictions.

Despite the limited available validation at full-scale, we believe it makes good sense to use a CFD tool to compare reactor performance whilst experimental techniques improve, and large-scale experiments are performed.

3. Results and discussion

3.1. Fluid dynamics

Fig. 3 shows the transient average velocity for the bubble column and stirred tank with Rushton impellers at benchmark conditions for the three different liquid volumes examined. As the simulations have been run at similar specific power inputs, the magnitude of the liquid velocity is similar for all three liquid volumes. Hence, only results for the 90 m^3 cases are subsequently plotted, as they are representative of the flow patterns found in the reactors. Although the flow pattern and magnitude were similar with different volumes, differences in mixing time and oxygen transfer values were observed. These are shown in Sections 3.2 and 3.3. In practice the specific power input may vary with time, depending on the operational strategy used. However, in this article we have chosen to keep the specific power input fixed as a function of time in order to understand the effect of the liquid volume on process performance.

Fig. 4 shows the effect of changing the volumetric power input on the transient average liquid velocity for the three reactor configurations examined at a volume of 90 m^3. In all cases, it was found that the same flow patterns were observed for the benchmark and low settings conditions, with the magnitude of the liquid velocity decreasing at lower volumetric power inputs. For example, flow in the bubble columns was characterised by upwards flow in the centre of the column and downwards flow at the walls, forming one large circulation cell. Contrastingly, the flow in the stirred tanks showed clear circulation loops around each impeller. When Rushton turbines are used, two main recirculation loops are observed at the top and the bottom of the impeller (Fig. 4B and E), following the characteristic profile of a radial impeller type. The A310 impellers have one axial loop at each impeller (Fig. 4C and F). These observations are in accordance with measurements in a 30 m^3 stirred tank with similar impeller configurations [4]. As shown in Fig. 3, the number of these zones increased with the liquid volume as the number of impellers also increased.

Comparison between the instantaneous liquid velocity for the bubble column and Rushton cases is given in Fig. 5. Results for the A310 impellers are similar to those shown for the Rushton impellers and hence have not been depicted. Fig. 5 also shows a plot of the variation in the velocity magnitude for the two different configurations, this has been calculated as the standard deviation of the velocity divided by the average velocity. As shown in Fig. 5, the flow in the bubble columns (A-C) is much less structured and the variation in the velocity magnitude is much higher than the stirred tank configuration (D and H). The structure in the stirred tank cases is largely due to the presence of the impellers which imposes a velocity field on the liquid phase and may act to dampen fluctuations due to the bubble plume. Contrastingly, flow patterns in the bubble column are entirely driven by the input of the air, and, at the relatively high superficial velocities used, there is significant fluctuation in the location of the bubble plume [31]. This leads to a less structured flow pattern, with a higher degree of time varying behaviour than the flow pattern inside the STR. Such results also suggest that the mixing time may be lower for the bubble column configuration, as the transient flow patterns may be more effective at uniformly dispersing a tracer throughout the reactor volume than the structured flow found for the stirred tank configurations. Finally, these results clearly demonstrate the need to solve these systems (particularly the bubble columns) as transients with relatively long averaging times.

The eddy dissipation rate (ε) quantifies the rate at which turbulence kinetic energy is dissipated in the liquid phase. From the perspective of bioreactor modelling, this is important for both mass transfer and the shear stress experienced by the cells. Plots of the transient average eddy dissipation rate for the three configurations examined are shown in Fig. 6.

It was observed that the local magnitude and distribution of the eddy dissipation rate depends on the reactor type. The bubble columns present a more homogeneous distribution of the eddy dissipation rate than the stirred tanks, with average values of 1 – 2 m^2 s^{-3} in most of the reactor volume with decreasing values (< 1 m^2 s^{-3}) near the walls (Fig. 6 A and D). These results are correlated with the location of the bubble plume (see Fig. 7), with higher levels of turbulence eddy dissipation rate being found where the gas volume fraction is higher. In stirred tank reactors, higher eddy dissipation rates (> 5 m^2 s^{-3}) are found in the vicinity of the impellers, while low values (< 0.5 m^2 s^{-3}) occur in most of the stator domain (Fig. 6B, C, E and F). The local eddy dissipation rate values did not show significant changes in the stator domain depending on the impeller type. Nevertheless, in the regions close to the impellers, higher local values of the eddy dissipation rate were found with RTD impellers than with hydrofoil A310 impellers (Fig. 6B, C, E and F). Such results are a consequence of the higher power number of Rushton impellers ($N_p = 5.5$) compared with the A310 hydrofoil configuration ($N_p = 0.3$) [3]. Similarly, higher values of the eddy dissipation rate were found at higher power inputs.

The final aspect to assess the fluid dynamics of the bioreactors studied is the evaluation of the gas volume fraction, which is relevant for oxygen transfer. The transient averages of the gas volume fraction for all cases studied at 90 m^3 are shown in Fig. 7. First, it is observed that higher gas volume fractions are achieved in the bubble columns (Fig. 7A and D) in comparison with the stirred tanks (Fig. 7B and E, C and F), at all simulated volumes. These gas hold-up ranges agree with those found in the literature (0.05–0.025 for stirred tanks [4,48] and 0.20–0.40 for bubble columns [30,31]).

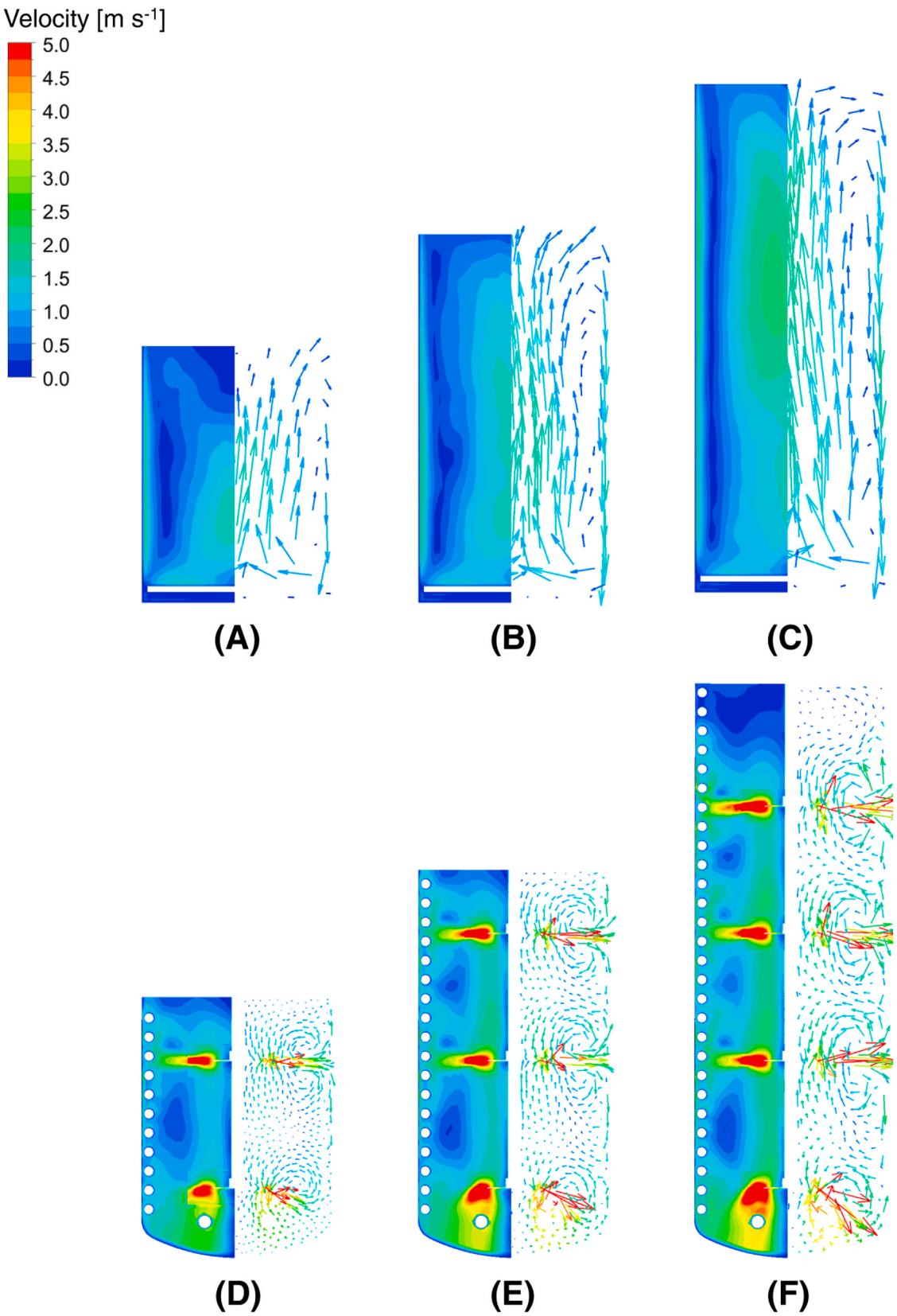

Fig. 3. Transient averages after 90 s of the velocity and the velocity in the stationary frame at volumes of 40 (A and D), 60 (B and E) and 90 (C and F) m^3 for the bubble column (A-C) and the stirred tank with RTD impellers (D–F) with benchmark operational conditions (Table 2). (The number of arrows plotted does not reflect the mesh density.).

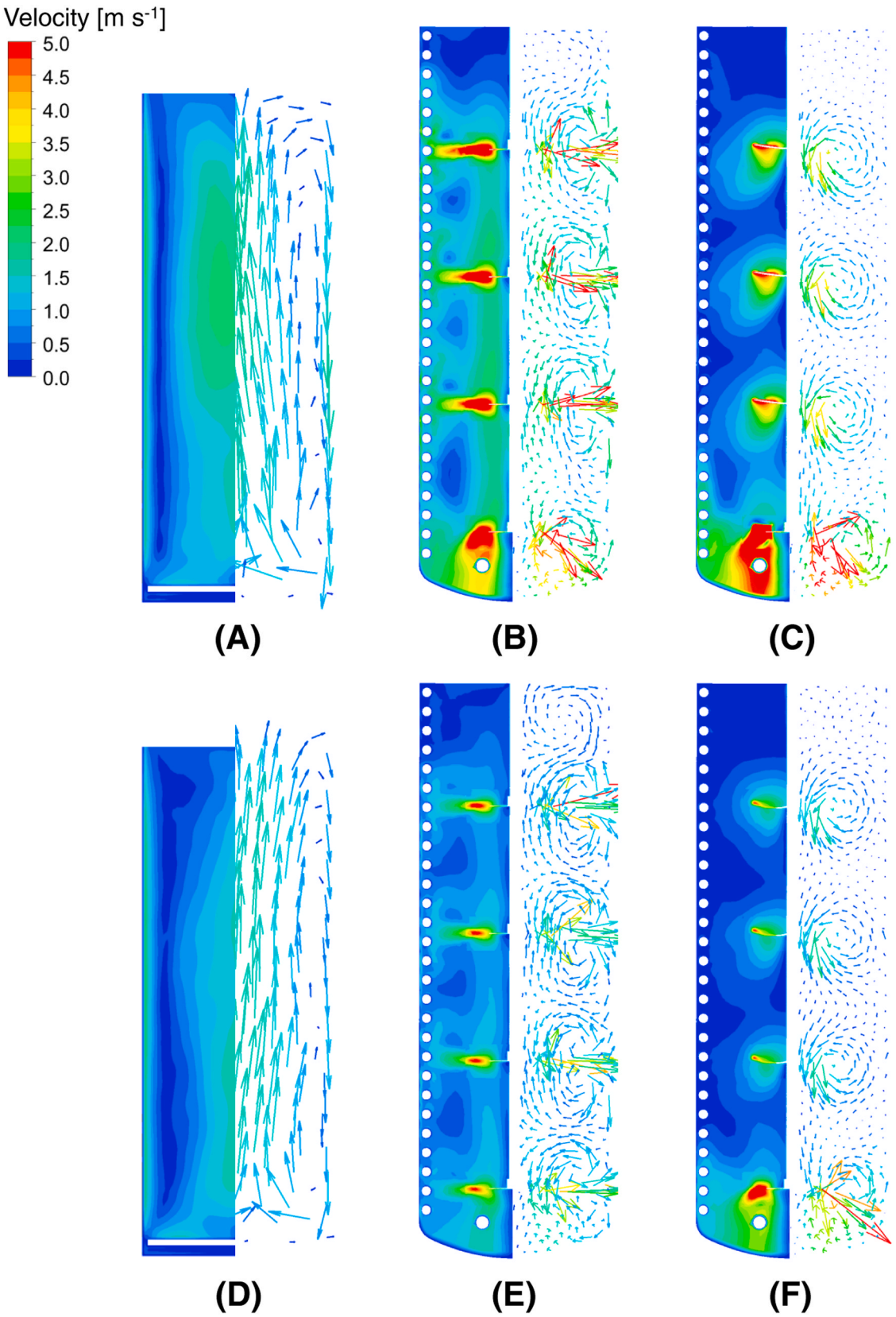

Fig. 4. Transient averages after 90 s of the velocity and velocity in the stationary frame at volumes of 90 m^3 for the bubble column (A and D) and the stirred tanks with RTD impellers (B and E) and hydrofoil A310 impellers (C and F) with benchmark (A-C) and low settings (D-F) operational conditions (Table 2). Benchmark conditions are operated with a power input per volume for agitation of 3.9 – 4 kW m^{-3}, aeration rates of 1.93 and 0.97 m s^{-1} for bubble columns and stirred tanks, respectively, and a headspace pressure of 1 bar for stirred tanks. Low settings are operated with a power input per volume for agitation of 0.8 – 0.9 kW m^{-3}, aeration rates of 0.97 and 0.40 m s^{-1} for bubble columns and stirred tanks, respectively and no additional headspace pressure. (The number of arrows plotted does not reflect the mesh density.).

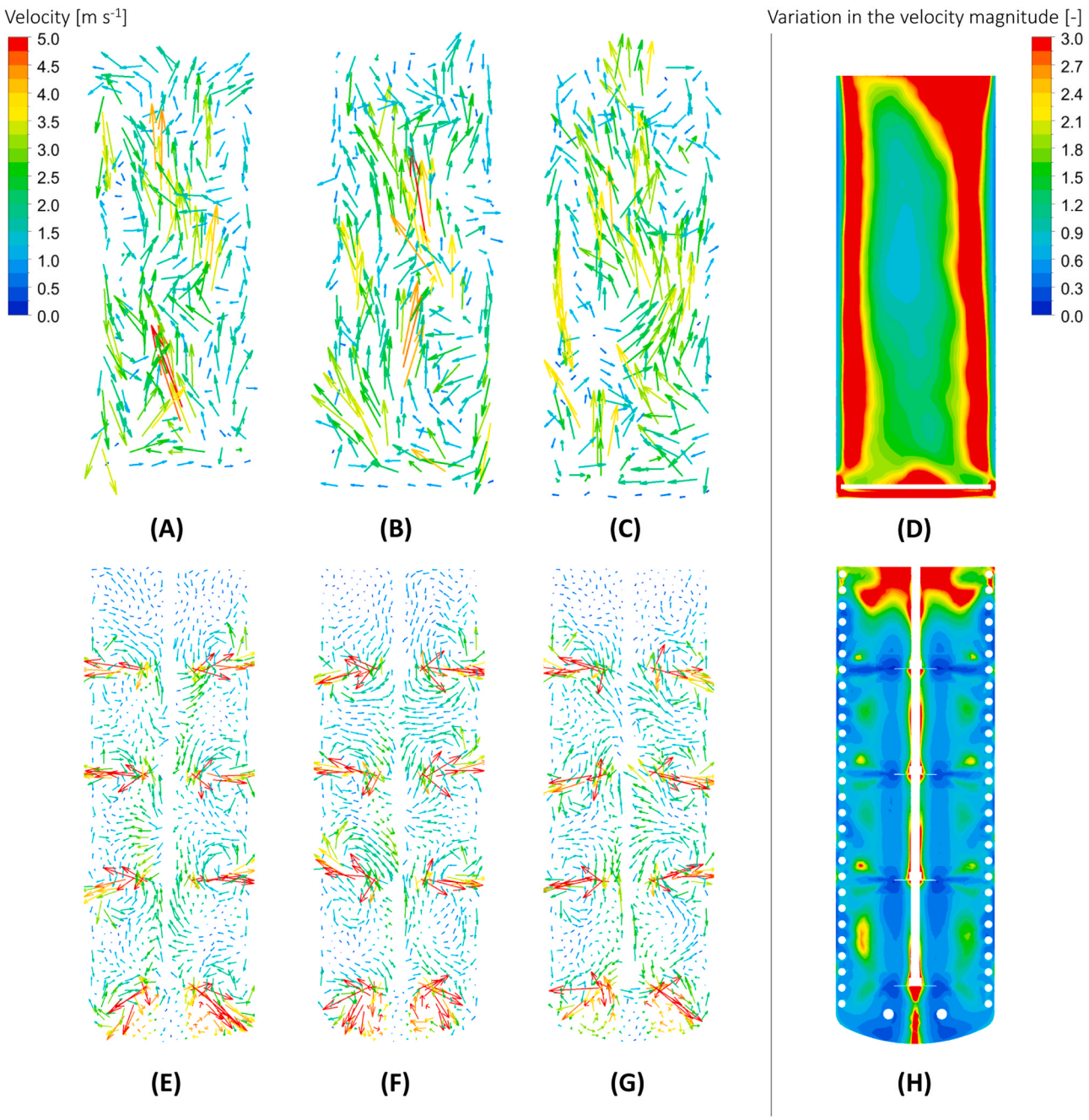

Fig. 5. Vector plots showing instantaneous liquid velocities for the bubble column (A-C) and stirred tank with Rushton turbine disk (RTD) impellers (E-G). All cases have a volume of 90 m^3 and are operated with benchmark conditions (Table 2). The snapshots in each row are spaced 10 s apart. Also shown are the velocity variations for the bubble column (D) and RTD (H) configurations. The velocity variation is defined as the standard deviation of the velocity divided by the average velocity.

As shown in Fig. 7, the gas volume fraction tended to increase with height for all configurations, this is due to the expansion of the gas with the reduction in pressure. For both the bubble column and stirred tank cases there was a zone below the sparger with a low gas volume fraction. Operating at higher power inputs minimised this volume for the stirred tank cases, while increasing the power input for the bubble column had relatively little effect (Fig. 7). These observations evidence the need to position the sparger at a low vertical point in the bioreactor, in order to prevent the occurrence of such dead spots, which can ultimately affect oxygen transfer and process performance.

3.2. *Mixing performance*

Fig. 8 gives a comparison between the mixing times calculated for the three different reactor configurations. For all configurations examined, the mixing time decreased as the volumetric power input increased (i.e., the mixing time was less for the benchmark conditions than for the low settings). This agrees with the results shown in Figs. 3 and 4, where the liquid velocity was found to increase as the volumetric power input increased. The magnitude of this change was less for the bubble column configurations, this being in line with the literature [19,21,49], where the mixing time is a relatively weak function of the superficial gas velocity (and hence the volumetric power input).

It was found that the mixing time increased as the liquid volume

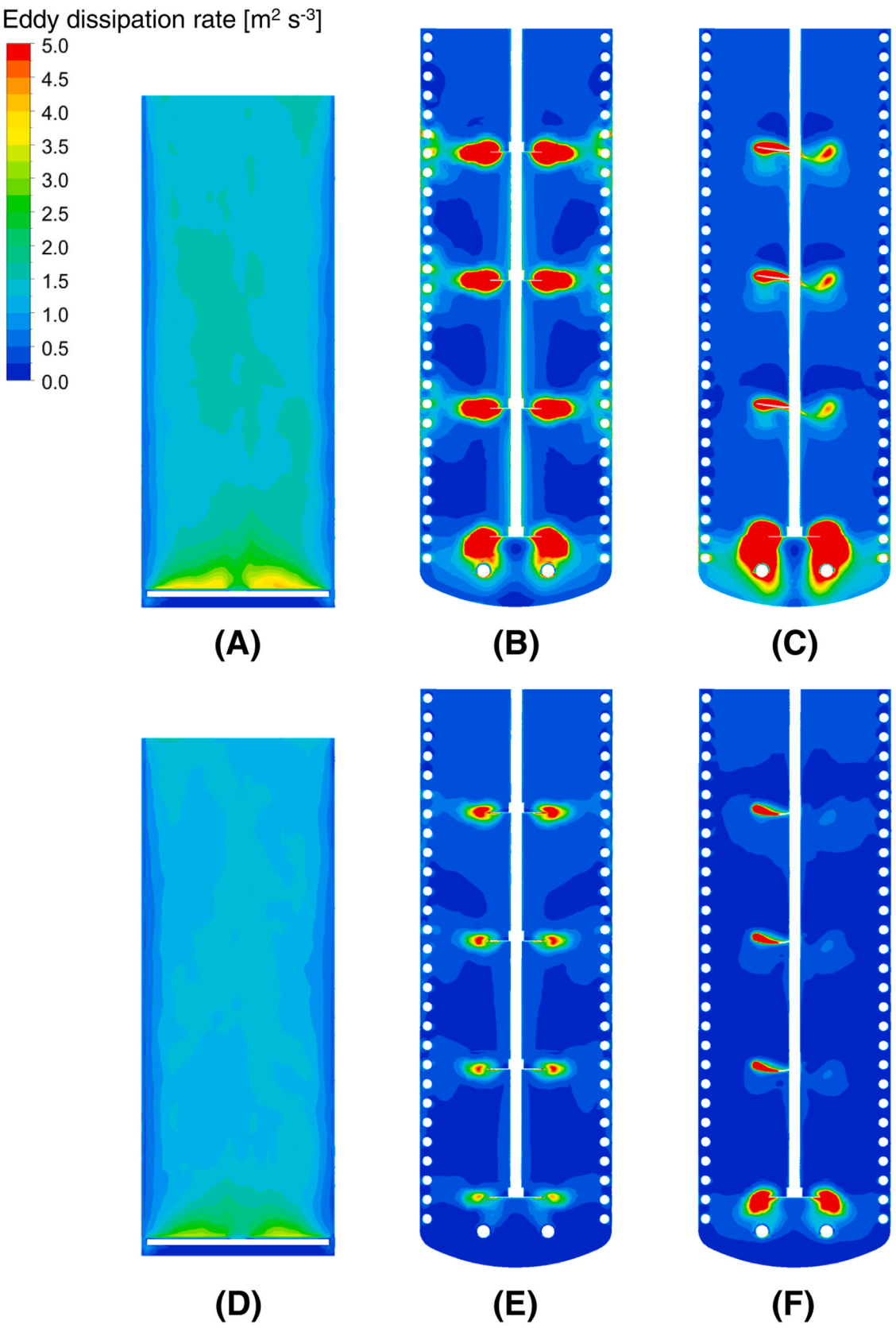

Fig. 6. Transient averages after 90 s of the eddy dissipation rate at volumes of 90 m^3 for the bubble column (A and D) and the stirred tanks with RTD impellers (B and E) and hydrofoil A310 impellers (C and F) with benchmark (A-C) and low settings (D-F) operational conditions (Table 2).

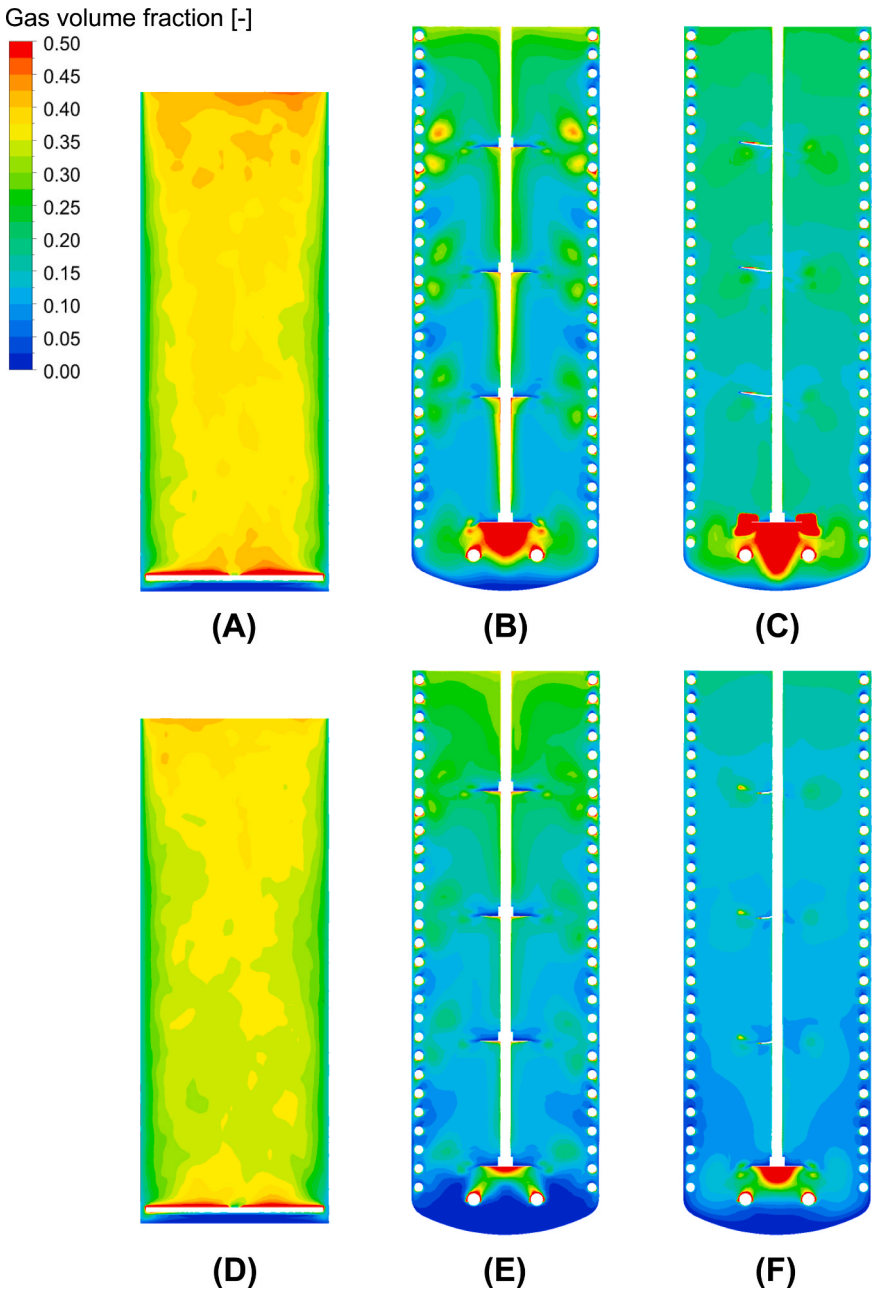

Fig. 7. Transient averages after 90 s of the gas volume fraction at volumes of 90 m^3 for the bubble column (A and D) and the stirred tanks with RTD impellers (B and E) and hydrofoil A310 impellers (C and F) with benchmark (A-C) and low settings (D-F) operational conditions (Table 2).

increased, with this being most pronounced for the stirred tank configurations. Again, this can be explained by the liquid velocity patterns shown in Figs. 3 and 4. As the liquid volume increases in a stirred tank, the number of circulation cells around the impellers increases, and the limiting step in the mixing process is the transfer between these circulation cells [4]. Contrastingly, the flow in the bubble column is much less structured and more transient (see Fig. 5), meaning that the changing liquid level has less effect on the mixing time as the oscillating bubble plume more quickly disperses the tracer throughout the liquid phase. This behaviour also explains why the mixing times in the bubble columns are substantially lower than that for the stirred tanks, with values ranging between 10 and 26 s for the bubble column and 14 and 204 s for the stirred tanks. The order of magnitude of these values agree with those calculated with correlations from the literature, corresponding to 1–18 s for bubble columns [21] and 91–597 s for STRs [50].

The mixing time values did not show a significant change depending on the impeller configuration (Fig. 8). When examining the velocity profiles for both cases studied (Fig. 4), it is observed that the re-circulation loops of the A310 configuration are rather isolated between them, resulting in high velocity values in the vicinity of the impeller and significant dead zones in terms of velocity in most of the reactor volume. The poor connection between re-circulating loops is likely to have challenged the efficient dispersion of the tracers in the liquid phase. In contrast, the multiple re-circulating loops of the RTD configuration provide higher local velocities and have a better connection, thus resulting in similar mixing time values than the A310 configuration. This observation underlines that one of the main challenges with mixing in stirred tanks with multiple impellers is the efficient connection between recirculation loops.

Finally, the utilisation of various feeding or monitoring positions did not lead to significantly different mixing time estimations. However, the addition of tracer at the top position seemed to increase the mixing time

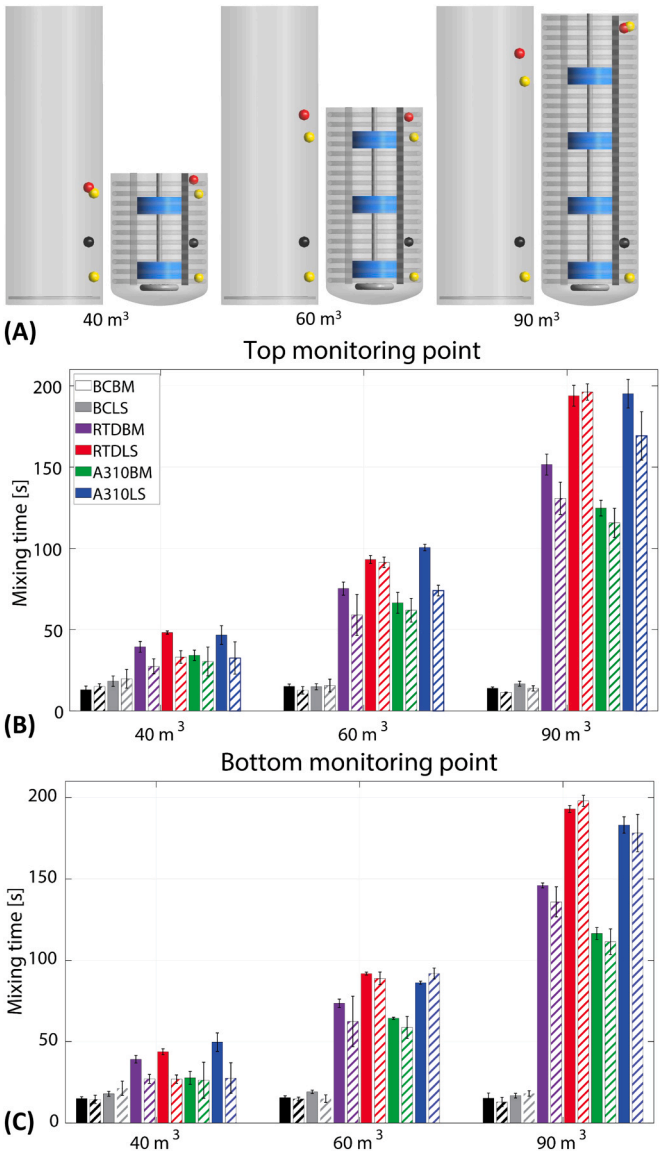

Fig. 8. Locations of the top (red sphere) and bottom (black sphere) feeding positions and the monitoring points (yellow spheres) at 40, 60 and 90 m^3 for bubble columns (left) and stirred tanks (right) for the calculation of the mixing time. The interface between tank and impeller domains are shown in blue (A). Mixing times estimated for the top (B) and bottom (C) monitoring points. Solid bars are for the top tracer addition point, while dashed bars are for the bottom tracer addition point. Reported values are the average, error bars denote one standard deviation about the mean. BC: bubble column, RTD: stirred tanks with RTD impellers, A310: stirred tanks with one STR impeller at the bottom and hydrofoil A310 impellers at the top, BM: benchmark conditions, LS: low settings conditions. Details of the operational conditions are found in Table 2.

in comparison with bottom feeding. This may be linked to the higher turbulence level at the bottom feeding position (as it is located between re-circulating loops) (Fig. 4), which ultimately improves mixing performance. Changing the feeding at the bottom position has already been shown to provide a more efficient substrate distribution in CFD simulations of industrial fermentation processes [51]. These results also illustrate the benefits of having a detailed understanding of the hydrodynamics from the perspective of optimising bioreactor designs.

3.3. Oxygen transfer

The oxygen transfer rate is a function of both the local gas volume fraction and the liquid film mass transfer coefficient (k_L). As shown in Fig. 7, the gas volume fraction is both higher and more uniformly distributed throughout the reactor for the bubble columns. The value of the liquid film mass transfer coefficient (k_L) depends on the bubble size, the eddy dissipation rate, the physical properties of the gas and liquid phase and the composition of the liquid phase [32,52–54]. A widely used correlation for k_L is that defined by Lamont and Scott [44], where the mass transfer coefficient is a function of the gas diffusivity, the rheology of the broth and the eddy dissipation rate (Eq. 15). This correlation has been used in many CFD simulations of industrial aerobic fermentation processes with stirred tank reactors [55,56], where it has been concluded to provide satisfactory estimates under typical fermentation process conditions. Here, the same correlation has been evaluated to calculate k_L in the different systems studied; contour plots of the transient averages at 90 m^3 are shown in Fig. 9.

As k_L is correlated with the eddy dissipation rate, the local distribution of k_L follows that of the turbulence eddy dissipation rate (see Fig. 6). Thus, the local distribution of k_L in bubble columns (Fig. 9A and D) is more homogeneous (2.8×10^{-4} – 6.3×10^{-4} m s^{-1}) than that of stirred tanks (Fig. 9B and D, C and F). In the latter, higher values (> 7×10^{-4} m s^{-1}) are found near the impellers in comparison with the rest of the fermenter (2.1×10^{-4} m s^{-1} – 3.5×10^{-4} m s^{-1}) because of the higher turbulence levels. Furthermore, transient volume-weighted averages of k_L in bubble columns were higher than in stirred tanks, ranging between 4.4×10^{-4} and 7×10^{-4} m s^{-1} and 3.1×10^{-4} and 4.7×10^{-4} m s^{-1}, respectively. The differences observed regarding the impeller type used and the operational conditions in terms of eddy dissipation rate (Fig. 6) are also found with the local k_L distribution (Fig. 9).

A challenge in using correlations for k_L based on values of the turbulence eddy dissipation rate is that RANS based turbulence models are likely to underestimate these values [57]. In this case the volume averaged power input was of the order 60% of the expected value for the stirred tank cases, suggesting that the value of k_L and hence the oxygen transfer rate is likely to be underpredicted. It may be possible to include an empirical factor in the model to correct for this. This could be done by multiplying the value of the turbulence eddy dissipation by an appropriate constant when calculating the value of k_L (Eq. 15). Such an approach has the advantages of simplicity and computational efficiency; however it may not be broadly applicable. Alternatively, use of Shear Stress Transport (SST) turbulence models has been shown to give improved predictions of the turbulence [57], however use of such models often necessitates a high mesh resolution, further adding to the already considerable computational demand required to simulate bioreactors. An avenue for future work would be the development of computationally efficient models capable of providing accurate predictions of the turbulence eddy dissipation rate.

Fermentation media contains a complex and often poorly defined mixture of compounds (e.g., proteins and antifoams) which have been shown to reduce the mass transfer (by approximately 3–5 fold) [22,43,54]. Hence, it may be necessary to take this into account when modelling such systems to obtain an accurate estimate of the oxygen transfer rate. To this end, the k_La has been determined using k_L values calculated using the Lamont and Scott [44] correlation, as well as using a fixed value of k_L (2×10^{-4} m s^{-1}), this corresponding to an experimentally measured [43] value for bubble columns containing a range of surfactants. A plot of the transient average k_La values for the different reactor configurations examined is presented in Fig. 10. The choice of the method used to determine k_L had a large impact on the calculated k_La values, with volume-weighted average values ranging between 192 and

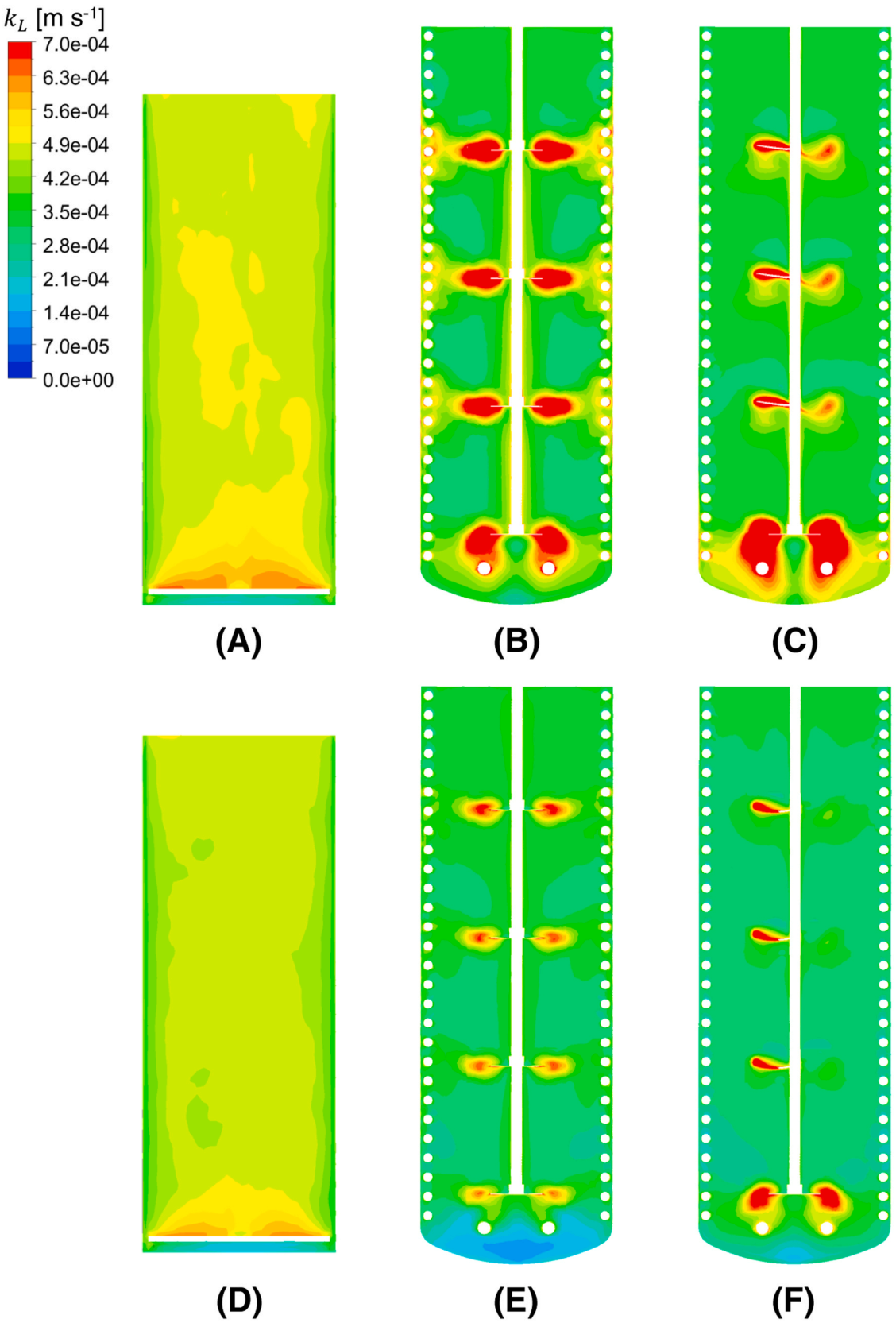

Fig. 9. Transient averages after 90 s of the mass transfer coefficient ($\mathbf{k_L}$) calculated with the Lamont and Scott correlation (Eq. 15) at volumes of 90 m^3 for the bubble column (A and D) and the stirred tanks with RTD impellers (B and E) and hydrofoil A310 impellers (C and F) with benchmark (A-C) and low settings (D-F) operational conditions (Table 2).

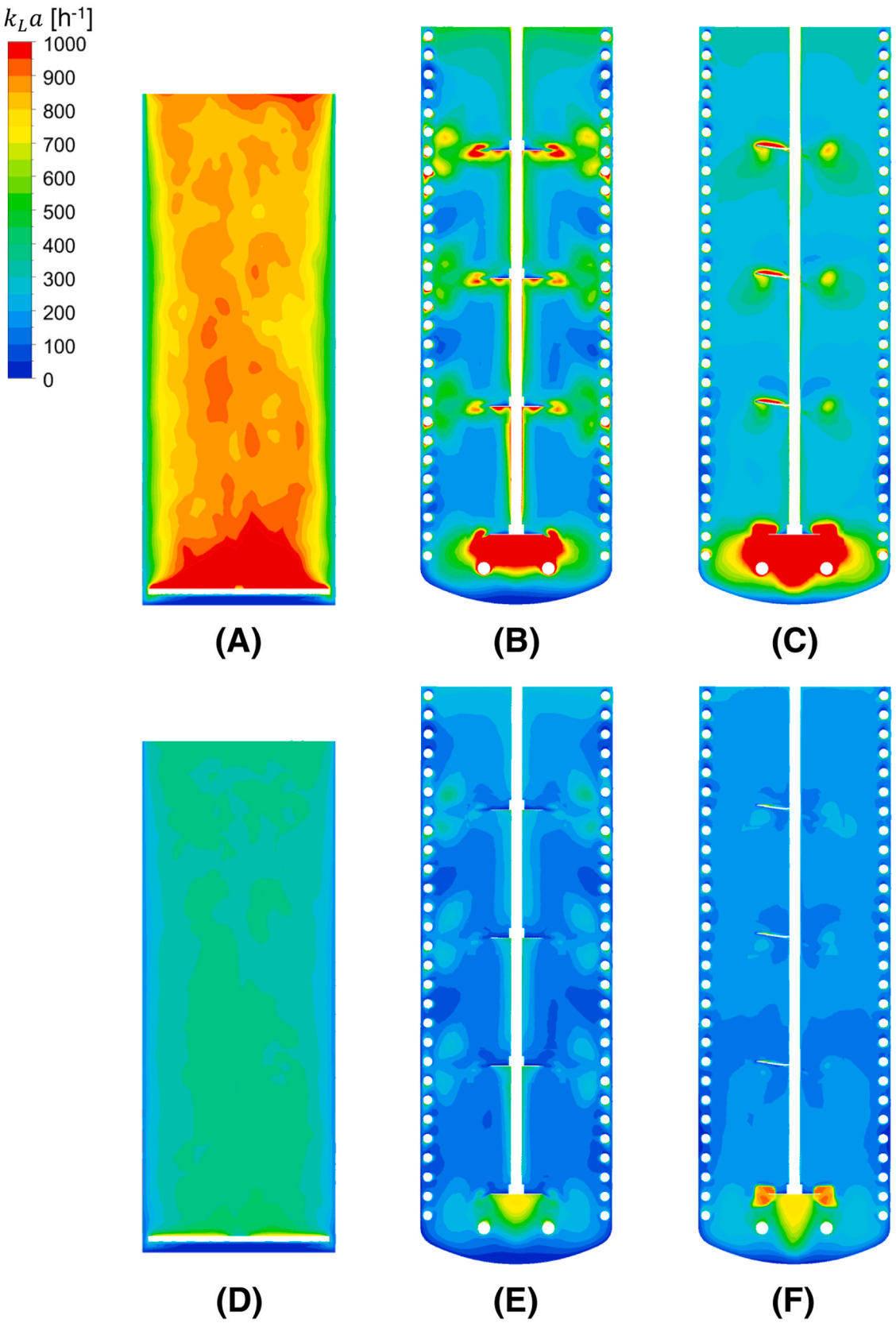

Fig. 10. Transient averages after 90 s of the overall mass transfer coefficient ($\mathbf{k_L a}$) calculated with the Lamont and Scott correlation (A-D, Eq. 15) and a fixed $\mathbf{k_L}$ value (D-F, 2 $\times 10^{-4}$ m s^{-1} [41]) at volumes of 90 m^3 for the bubble column (A and D) and the stirred tanks with RTD impellers (B and E) and hydrofoil A310 impellers (C and F) with benchmark operational conditions (Table 2).

1038 h^{-1}, using the Lamont and Scott correlation, and 109 and 436 h^{-1}, using the fixed value of k_L (2×10^{-4} m s^{-1}). These values are in line with those experimentally measured by others [46,58] at similar conditions. Furthermore, when the Lamont and Scott correlation was used, it was found that the overall k_La values were higher for the bubble column, due to the higher gas volume fractions and k_L values. Literature values from fermentation processes performed with in industrial stirred tank reactors match with the values calculated in this article, strengthening its modelling choices. These correspond to 144–180 h^{-1} with P_i/V_L of 1.8–2 kW m^{-3} [7,16], and 500 h^{-1} with P_i/V_L of 1.8 kW m^{-3} [55].

In practice the k_La values shown in Fig. 10 are likely to represent reasonable estimates of the upper and lower bounds of what is found in large-scale bioreactors. Actual values are likely to be a function of the medium composition, microorganism and the fermentation time (as the composition of the liquid phase can change). Here it is also important to note that the CFD model used neglected bubble break-up and coalescence, and hence may not accurately predict the interfacial area if such phenomena are important. However, use of more complex CFD models is complicated by the fact that available models for bubble break-up and coalescence generally have poor predictive ability [38,59,60] and add considerable computational burden. Given that this is the case it is difficult to justify the use of such models. This also underscores the need for data from industrial-scale equipment which can be used to the further development and validation of CFD models.

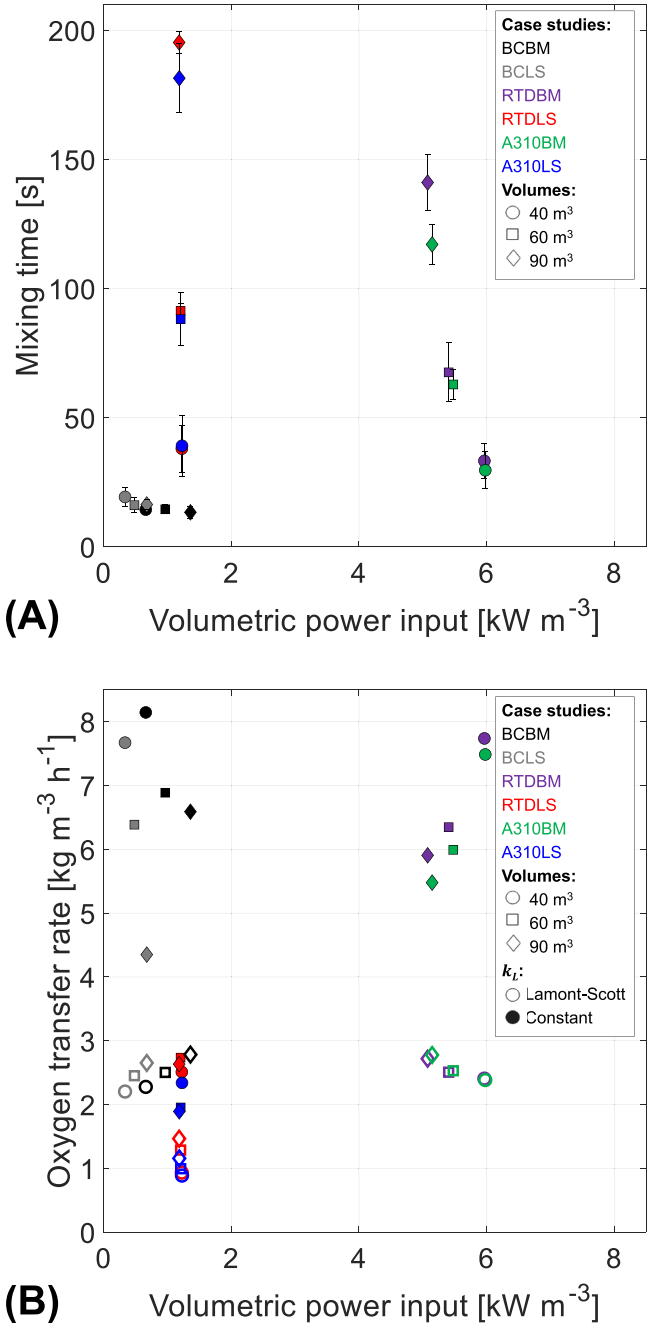

Fig. 11. Plot showing the mixing time (A) and oxygen transfer rate (B) as a function of the volumetric power input for all systems simulated. In panel (B) $\mathbf{k_L}$ was assumed to be either a constant value (2×10^{-4} m s^{-1}) [41], (shown as filled markers) or calculated with the Lamont and Scott correlation [42] (shown as open markers).

3.4. Comparison between bioreactor designs

A comparison of the discussed variables for the reactor types studied is shown in Fig. 11, where the mixing time and the oxygen transfer rate are plotted as functions of the total volumetric power input (i.e., taking into account both agitation, air compression and the effect of the headspace pressure (if applicable)). The average mixing time and its standard deviation for each reactor type and volume were calculated considering all the values simulated for that case study (i.e., all top and bottom feeding and monitoring positions). The oxygen transfer rate values were estimated by multiplying the volume-weighted average k_La over the entire reactor volume with the volume-weighted average oxygen concentration gradient, as described in Eq. (1). The dissolved oxygen concentration was assumed to be 20% of the saturation value, as it is a reasonable set point in industrial aerobic fed-batch fermentation processes [39,61]. Both approaches previously discussed to calculate the k_L were tested for the calculation of the OTR, corresponding to the utilisation of a constant value (2×10^{-4} m s^{-1}) [43] and of a correlation from the literature [44]. This was done with the aim of calculating a realistic range for OTRs in industrial bioreactors given the uncertainty in determining the value of k_L.

Examination of Fig. 11A shows that the bubble column is a much more efficient configuration from a mixing perspective than the stirred tanks, with the calculated mixing times being much lower than those found in the stirred tanks at similar power inputs. The bubble column configuration also had the advantage that the mixing time did not markedly increase with the liquid volume, unlike the stirred tanks. As previously discussed, the differences in mixing behaviour are due to the different flow structures within the reactors, with the less structured and more transient flow found in the bubble column being advantageous from a mixing perspective. From the perspective of bioprocess scale-up bubble column reactors may be favoured as the lower mixing time will minimise gradients (e.g., of substrate concentration), which can lead to improved process performance [5–8]. As noted elsewhere [25] bubble columns have lower capital costs compared with stirred tanks (due to their mechanical simplicity), and this combined with their improved mixing performance may mean they are the more suitable configuration, particularly for large (> 100 m^3) fermentations. However, bubble columns are generally limited to processes where the liquid is Newtonian and has a relatively low viscosity (of the order 2×10^{-3} Pa s [25]). Here it must be noted that the conclusions found in this work only apply to low viscosity, Newtonian fermentation media, and that the conclusions are likely to differ for systems with more complex rheology.

Fig. 11B shows that the oxygen transfer rate ranged between 1 and 8 kg m^{-3} h^{-1}. There was a considerable variation in predictions of the OTR due to the uncertainty in calculating the value of k_L. Following the Lamont and Scott approach for the calculation of k_L (the open symbols in Fig. 11B), increasing the volumetric power input leads to an increase in the OTR. Both bubble columns and stirred tanks were predicted to achieve comparable OTR values with both k_L assumptions, with the bubble columns requiring a lower volumetric power input to achieve these values. This difference is directly related to the behaviour shown in Fig. 6 where bubble columns have higher average values of the

turbulence eddy dissipation rate, despite the stirred tanks having higher values in the vicinity of the impellers. The more uniform distribution of power in bubble columns leads to higher predictions of k_L using the model of Lamont and Scott [44] as the values are proportional to the turbulence eddy dissipation rate. This combined with the higher gas hold-up (and hence higher interfacial area) in the bubble columns leads to the model predicting relatively high values of the OTR. In comparison it was found to be possible to achieve similar values (6–8 kg m^{-3} h^{-1}) using the stirred tanks, but this necessitated higher power inputs from both agitation and gas compression (due to the backpressure applied). It was found that the OTR was marginally higher for the Rushton configuration, due to the higher power number of these impellers leading to a higher average k_L value.

As previously noted, the composition and physical properties of the liquid phase can significantly affect mass transfer [12,22,23], for many industrial processes the composition and properties of the medium can also change over the course of a batch. For example, it was found for all cases for which k_L was calculated with the Lamont and Scott correlation [44] that the OTR decreased as the liquid volume increased (Fig. 11B), this being due to the higher viscosity used at higher volumes. To understand the potential effect of surfactants (e.g. antifoam agents) a fixed value (2×10^{-4} m s^{-1}) [43] was used when calculating k_L, the effect of this on the OTR is shown in Fig. 11 C. Predicted OTR values ranged from 1 to 3 kg m^{-3} h^{-1}, with the higher gas volume fraction in the bubble columns compensating for the increased backpressure (and hence higher driving force) in the stirred tanks run at benchmark conditions.

Predicted OTR values for the same configuration and operating conditions were found to differ by a factor of 2–4; with the values in this work providing estimates for the minimum and maximum values achievable. From a mass transfer perspective, the higher gas volume fraction (see Fig. 7) found in bubble columns seems advantageous when compared with stirred tanks. Nevertheless, it is the manner how k_L is to be calculated in each reactor type that will determine the actual OTR levels. Making accurate predictions of the OTR relies on knowledge of the composition and properties of the liquid phase and how these factors affect k_L. These values are likely to be process specific (e.g. different approaches to calculate k_L depending on the reactor type), and this also highlights the need for measurements made under industrial operating conditions for model validation.

4. Conclusions

The aims of this work were to use CFD modelling to quantify the performance of different large-scale bioreactor designs resembling typical industrial operational conditions, as despite its industrial significance relatively little information about this is available in the open literature. The assessment of the fluid dynamics, mixing performance and oxygen transfer of the different cases studied lead to the two following conclusions. It must be noted that the rheology studied in this article corresponds to Newtonian fluids, and that different results regarding mass transfer and mixing might arise when investigating flows with different rheology.

Firstly, it was concluded that bubble columns have more efficient mixing than stirred tanks, with mixing time differences of up to one order of magnitude with significantly lower volumetric power input values. This is a consequence of the highly transient behaviour of bubble columns, which facilitates mixing.

Secondly, it was observed that there was considerable uncertainty in the predictions of the OTR, with predicted values for the same configuration varying by a factor of 2–4 depending on the method used to determine the value of the liquid film mass transfer coefficient (k_L). Without reliable, industrial scale data it is difficult to determine which methodology is most appropriate. Hence, having access to industrial-scale OTR measurements is key to the development and validation of CFD models. When comparing between the different reactor designs it was found that the higher gas volume fraction and more uniform spatial distribution of the turbulence eddy dissipation led to more efficient oxygen transfer in bubble columns, a conclusion in line with that of others [24].

In summary, results from this publication provide a detailed hydrodynamic characterisation of industrial scale bioreactors. These results can be used to compare different reactor configurations, and additionally the CFD models developed here can form the basis for more complex models which account for the microbial kinetics. Future work in this direction should also systematically examine the same flow variables in systems with more challenging rheology (e.g., viscous and/or non-Newtonian broths) to yield a complete portrayal of the fluid dynamics, mixing performance and oxygen transfer in industrial fermentation processes.

CRediT authorship contribution statement

Gisela Nadal-Rey: writing - original manuscript and writing - reviewing and editing, Conceptualization, Modelling, CFD simulations, Data analysis, Writing. **Dale D. McClure:** writing - original manuscript and writing - reviewing and editing, Conceptualization, Modelling, CFD simulations, Data analysis, Writing. **John M. Kavanagh**: Supervision, Writing – review and editing. **Benny Cassells**, Supervision, Writing – review and editing. **Sjef Cornelissen**: Supervision, Writing – review and editing. **David F. Fletcher** Conceptualization, Supervision, Writing – review and editing. **Krist V. Gernaey**: Supervision, Writing – review and editing.

Declaration of Competing Interest

The authors declare that they have no known competing financial interests or personal relationships that could have appeared to influence the work reported in this paper.

Acknowledgments

This work was supported by the Technical University of Denmark and Novozymes A/S. The authors acknowledge the DTU Computing Center, the Sydney Informatics Hub and the University of Sydney's high-performance computing cluster, Artemis, for providing the computing resources that have contributed to the results reported herein.

Appendix A. Supporting information

Supplementary data associated with this article can be found in the online version at doi:10.1016/j.bej.2021.108265.

References

[1] P.M. Doran, Bioprocess Engineering Principles, Elsevier Science & Technology, Waltham, MA, 2012.
[2] J. Villadsen, J.H. Nielsen, G. Lidén. Bioreaction Engineering Principles, third ed., Springer, US, Boston, MA, 2011.
[3] E.L. Paul, V.A. Atiemo-Obeng, S.M. Kresta, Handbook of Industrial Mixing: Science and Practice, John Wiley & Sons, 2004.
[4] P. Vrábel, R.G.J.M. van der Lans, K.C.A.M. Luyben, L. Boon, A.W. Nienow, Mixing in large-scale vessels stirred with multiple radial or radial and axial up-pumping impellers: modelling and measurements, Chem. Eng. Sci. 55 (2000) 5881–5896.
[5] S.O. Enfors, M. Jahic, A. Rozkov, B. Xu, M. Hecker, B. Jürgen, E. Krüger, T. Schweder, G. Hamer, D. O'Beirne, N. Noisommit-Rizzi, M. Reuss, L. Boone, C. Hewitt, C. McFarlane, A. Nienow, T. Kovacs, C. Trägårdh, L. Fuchs, J. Revstedt, P.C. Friberg, B. Hjertager, G. Blomsten, H. Skogman, S. Hjort, F. Hoeks, H.Y. Lin, P. Neubauer, R. van der Lans, K. Luyben, P. Vrabel, Å. Manelius, Physiological responses to mixing in large scale bioreactors, J. Biotechnol. 85 (2001) 175–185.
[6] S. George, G. Larsson, K. Olsson, S.O. Enfors, Comparison of the Baker's yeast process performance in laboratory and production scale, Bioprocess Biosyst. Eng. 18 (1998) 135–142.
[7] F. Bylund, E. Collet, S.O. Enfors, G. Larsson, Substrate gradient formation in the large-scale bioreactor lowers cell yield and increases by-product formation, Bioprocess Eng. 18 (1998) 171–180.

[8] G. Larsson, M. Törnkvist, E.S. Wernersson, C. Trägårdh, H. Noorman, S.O. Enfors, Substrate gradients in bioreactors: origin and consequences, Bioprocess Biosyst. Eng. 14 (1996) 281–289.

[9] N. Kantarci, F. Borak, K.O. Ulgen, Bubble column reactors, Process Biochem. 40 (2005) 2263–2283.

[10] A. Rosseburg, J. Fitschen, J. Wutz, T. Wucherpfennig, M. Schlüter, Hydrodynamic inhomogeneities in large scale stirred tanks – Influence on mixing time, Chem. Eng. Sci. 188 (2018) 208–220.

[11] M. Jamialahmadi, C. Branch, H. Müller-Steinhagen, Terminal bubble rise velocity in liquids, Chem. Eng. Res. Des. 72a (1994) 119–122.

[12] Y. Kawase, M. Moo-Young, The effect of antifoam agents on mass transfer in bioreactors, Bioprocess Biosyst. Eng. 5 (1990) 169–173.

[13] G. Nadal-Rey, D.D. McClure, J.M. Kavanagh, S. Cornelissen, D.F. Fletcher, K. V. Gernaey, Understanding gradients in industrial bioreactors, Biotechnol. Adv. 46 (2021), 107660.

[14] D.D. McClure, J.M. Kavanagh, D.F. Fletcher, G.W. Barton, Characterizing bubble column bioreactor performance using computational fluid dynamics, Chem. Eng. Sci. 144 (2016) 58–74.

[15] C. Haringa, R.F. Mudde, H.J. Noorman, From industrial fermentor to CFD-guided downscaling: what have we learned? Biochem. Eng. J. 140 (2018) 57–71.

[16] C. Haringa, A.T. Deshmukh, R.F. Mudde, H.J. Noorman, Euler-Lagrange analysis towards representative down-scaling of a 22 m^3 aerobic S. cerevisiae fermentation, Chem. Eng. Sci. 170 (2017) 653–669.

[17] F. Siebler, A. Lapin, M. Hermann, R. Takors, The impact of CO gradients on *C. ljungdahlii* in a 125 m^3 bubble column: Mass transfer, circulation time and lifeline analysis, Chem. Eng. Sci. 207 (2019) 410–423.

[18] J.S. Crater, J.C. Lievense, Scale-up of industrial microbial processes, FEMS Microbiol. Lett. 365 (2018), fny138.

[19] D.D. McClure, N. Aboudha, J.M. Kavanagh, D.F. Fletcher, G.W. Barton, Mixing in bubble column reactors: Experimental study and CFD modeling, Chem. Eng. J. 264 (2015) 291–301.

[20] A.B. Pandit, J.B. Joshi, Mixing in mechanically agitated gas-liquid contactors, bubble columns and modified bubble columns, Chem. Eng. Sci. 38 (1983) 1189–1215.

[21] Y. Kawase, M. Moo-Young, Mixing time in bioreactors, J. Chem. Technol. Biotechnol. 44 (1989) 63–75.

[22] D.D. McClure, M. Lamy, L. Black, J.M. Kavanagh, G.W. Barton, An experimental investigation into the behaviour of antifoaming agents, Chem. Eng. Sci. 160 (2017) 269–274.

[23] F. Vardar-Sukan, Foaming: consequences, prevention and destruction, Biotechnol. Adv. 16 (1998) 913–948.

[24] D. Humbird, R. Davis, J.D. McMillan, Aeration costs in stirred-tank and bubble column bioreactors, Biochem. Eng. J. 127 (2017) 161–166.

[25] J. Crater, C. Galleher, J. Lievense, Consultancy on Large-Scale Submerged Aerobic Cultivation Process Design-Final Technical Report: February 1, 2016-June 30, 2016, National Renewable Energy Lab.(NREL), Golden, CO (United States), 2017.

[26] C. Bach, Modelling of Gradients in Large Scale Bioreactors, Department of Chemical and Biochemical Engineering, Technical University of Denmark, Kgs. Lyngby, 2018.

[27] E. Ertekin, J.M. Kavanagh, D.F. Fletcher, D.D. McClure, Validation studies to assist in the development of scale and system independent CFD models for industrial bubble columns, Chem. Eng. Res. Des. 171 (2021) 1–12.

[28] A.D. Burns, T. Frank, I. Hamill, J.-M. Shi, The Favre Averaged Drag Model for Turbulent Dispersion in Eulerian Multi-Phase Flows, in: Proceedings of the 5th International Conference on Multiphase FlowYokohama, Japan, 2004.

[29] D.F. Fletcher, D.D. McClure, J.M. Kavanagh, G.W. Barton, CFD simulation of industrial bubble columns: Numerical challenges and model validation successes, Appl. Math. Model. 44 (2017) 25–42.

[30] D.D. McClure, H. Norris, J.M. Kavanagh, D.F. Fletcher, G.W. Barton, Towards a CFD model of bubble columns containing significant surfactant levels, Chem. Eng. Sci. 127 (2015) 189–201.

[31] D.D. McClure, H. Norris, J.M. Kavanagh, D.F. Fletcher, G.W. Barton, Validation of a computationally efficient computational fluid dynamics (CFD) model for industrial bubble column bioreactors, Ind. Eng. Chem. Res. 53 (2014) 14526–14543.

[32] R. Clift, J.R. Grace, M.E. Weber, Bubbles, Drops and Particles, Academic Press, New York, 1978.

[33] M. Simonnet, C. Gentric, E. Olmos, N. Midoux, Experimental determination of the drag coefficient in a swarm of bubbles, Chem. Eng. Sci. 62 (2007) 858–866.

[34] M. Ishii, N. Zuber, Drag coefficient and relative velocity in bubbly, droplet or particulate flows, AIChE J. 25 (1979) 843–855.

[35] Ansys, CFX User's Manual, 2020.

[36] W. Yao, C. Morel, Volumetric interfacial area prediction in upward bubbly two-phase flow, Int. J. Heat Mass Transf. 47 (2004) 307–328.

[37] D.D. McClure, J.M. Kavanagh, D.F. Fletcher, G.W. Barton, Development of a CFD model of bubble column bioreactors: part one – a detailed experimental study, Chem. Eng. Technol. 36 (2013) 2065–2070.

[38] Z. Huang, D.D. McClure, G.W. Barton, D.F. Fletcher, J.M. Kavanagh, Assessment of the impact of bubble size modelling in CFD simulations of alternative bubble column configurations operating in the heterogeneous regime, Chem. Eng. Sci. 186 (2018) 88–101.

[39] L. Mears, S.M. Stocks, M.O. Albaek, G. Sin, K.V. Gernaey, Application of a mechanistic model as a tool for on-line monitoring of pilot scale filamentous fungal fermentation processes—The importance of evaporation effects, Biotechnol. Bioeng. 114 (2017) 589–599.

[40] M. Reuß, D. Josić, M. Popović, W.K. Bronn, Viscosity of yeast suspensions, Eur. J. Appl. Microbiol. Biotechnol. 8 (1979) 167–175.

[41] H. Singh, D.F. Fletcher, J.J. Nijdam, An assessment of different turbulence models for predicting flow in a baffled tank stirred with a Rushton turbine, Chem. Eng. Sci. 66 (2011) 5976–5988.

[42] D.A. Kouremenos, K.A. Antonopoulos, Isentropic exponents of real gases and application for the air at temperatures from 150 K to 450 K, Acta Mech. 65 (1987) 81–99.

[43] D.D. McClure, A.C. Lee, J.M. Kavanagh, D.F. Fletcher, G.W. Barton, Impact of surfactant addition on oxygen mass transfer in a bubble column, Chem. Eng. Technol. 38 (2015) 44–52.

[44] J.C. Lamont, D.S. Scott, An eddy cell model of mass transfer into the surface of a turbulent liquid, AIChE J. 16 (1970) 513–519.

[45] D.D. McClure, J.M. Kavanagh, D.F. Fletcher, G.W. Barton, Development of a CFD model of bubble column bioreactors: part two – comparison of experimental data and CFD predictions, Chem. Eng. Technol. 37 (2014) 131–140.

[46] D.D. McClure, J.M. Kavanagh, D.F. Fletcher, G.W. Barton, Oxygen transfer in bubble columns at industrially relevant superficial velocities: experimental work and CFD modelling, Chem. Eng. J. 280 (2015) 138–146.

[47] C. Bach, J. Yang, H. Larsson, S.M. Stocks, K.V. Gernaey, M.O. Albaek, U. Krühne, Evaluation of mixing and mass transfer in a stirred pilot scale bioreactor utilizing CFD, Chem. Eng. Sci. 171 (2017) 19–26.

[48] A.A. Yawalkar, V.G. Pangarkar, A.A. Beenackers, Gas hold-up in stirred tank reactors, Can. J. Chem. Eng. 80 (2002) 158–166.

[49] J. Tramper, K. Van't Riet, Basic Bioreactor Design, M. Dekker, New York, 1991.

[50] A.W. Nienow, Hydrodynamics of stirred bioreactors, Appl. Mech. Rev. 51 (1998) 3–32.

[51] C. Haringa, W. Tang, G. Wang, A.T. Deshmukh, W.A. van Winden, J. Chu, W. M. van Gulik, J.J. Heijnen, R.F. Mudde, H.J. Noorman, Computational fluid dynamics simulation of an industrial *P. chrysogenum* fermentation with a coupled 9-pool metabolic model: towards rational scale-down and design optimization, Chem. Eng. Sci. 175 (2018) 12–24.

[52] Y. Kawase, M. Moo-Young, Mathematical models for design of bioreactors: applications of: Kolmogoroff's theory of isotropic turbulence, Chem. Eng. J. 43 (1990) B19–B41.

[53] Y. Kawase, B. Halard, M. Moo-Young, Theoretical prediction of volumetric mass transfer coefficients in bubble columns for Newtonian and non-Newtonian fluids, Chem. Eng. Sci. 42 (1987) 1609–1617.

[54] A. Prins, K. van't Riet, Proteins and surface effects in fermentation: foam, antifoam and mass transfer, Trends Biotechnol. 5 (1987) 296–301.

[55] J. Morchain, J.-C. Gabelle, A. Cockx, A coupled population balance model and CFD approach for the simulation of mixing issues in lab-scale and industrial bioreactors, AIChE J. 60 (2014) 27–40.

[56] C. Haringa, W. Tang, A.T. Deshmukh, J. Xia, M. Reuss, J.J. Heijnen, R.F. Mudde, H. J. Noorman, Euler-Lagrange computational fluid dynamics for (bio)reactor scale down: an analysis of organism lifelines, Eng. Life Sci. 16 (2016) 652–663.

[57] G.L. Lane, Improving the accuracy of CFD predictions of turbulence in a tank stirred by a hydrofoil impeller, Chem. Eng. Sci. 169 (2017) 188–211.

[58] J.J. Heijnen, K. Van't Riet, Mass transfer, mixing and heat transfer phenomena in low viscosity bubble column reactors, Chem. Eng. J. 28 (1984) B21–B42.

[59] G. Besagni, F. Inzoli, T. Ziegenhein, D. Lucas, Computational Fluid-Dynamic modeling of the pseudo-homogeneous flow regime in large-scale bubble columns, Chem. Eng. Sci. 160 (2017) 144–160.

[60] R. Rzehak, T. Ziegenhein, S. Kriebitzsch, E. Krepper, D. Lucas, Unified modeling of bubbly flows in pipes, bubble columns, and airlift columns, Chem. Eng. Sci. 157 (2017) 147–158.

[61] O. Johnsson, J. Andersson, G. Lidén, C. Johnsson, T. Hägglund, Feed rate control in fed-batch fermentations based on frequency content analysis, Biotechnol. Prog. 29 (2013) 817–824.